

This is a repository copy of *B-cell Zone Reticular Cell Microenvironments Shape CXCL13 Gradient Formation*.

White Rose Research Online URL for this paper:

<https://eprints.whiterose.ac.uk/id/eprint/158426/>

Version: Accepted Version

---

**Article:**

Coles, Mark Christopher orcid.org/0000-0001-8079-9358, O'Toole, Peter John orcid.org/0000-0001-5295-2001, Lacey, Charles John Nash orcid.org/0000-0001-9250-2638 et al. (28 more authors) (2020) B-cell Zone Reticular Cell Microenvironments Shape CXCL13 Gradient Formation. Nature Communications. 3677. ISSN: 2041-1723

<https://doi.org/10.1038/s41467-020-17135-2>

---

**Reuse**

Items deposited in White Rose Research Online are protected by copyright, with all rights reserved unless indicated otherwise. They may be downloaded and/or printed for private study, or other acts as permitted by national copyright laws. The publisher or other rights holders may allow further reproduction and re-use of the full text version. This is indicated by the licence information on the White Rose Research Online record for the item.

**Takedown**

If you consider content in White Rose Research Online to be in breach of UK law, please notify us by emailing [eprints@whiterose.ac.uk](mailto:eprints@whiterose.ac.uk) including the URL of the record and the reason for the withdrawal request.



34    **ABSTRACT**

35    Through the formation of concentration gradients, morphogens drive graded responses to  
36    extracellular signals, thereby fine-tuning cell behaviors in complex tissues. Here we show that  
37    the chemokine CXCL13 forms both soluble and immobilized gradients. Specifically,  
38    CXCL13<sup>+</sup> follicular reticular cells form a small-world network of guidance structures, with  
39    computer simulations and optimization analysis predicting that immobilized gradients created  
40    by this network promote B cell trafficking. Consistent with this prediction, imaging analysis  
41    show that CXCL13 binds to extracellular matrix components in situ, constraining its  
42    diffusion. CXCL13 solubilization requires the protease cathepsin B that cleaves CXCL13 into  
43    a stable product. Mice lacking cathepsin B display aberrant follicular architecture, a  
44    phenotype associated with effective B cell homing to but not within lymph nodes. Our data  
45    thus suggest that reticular cells of the B cell zone generate microenvironments that shape both  
46    immobilized and soluble CXCL13 gradients.

47

48

49

50

51

52

53

54

55

56

57

58

59

60

## 61 INTRODUCTION

62

63 Non-hematopoietic stromal cells regulate the development and maintenance of niches within  
64 lymphoid tissues to support the retention, activation and proliferation of adaptive immune  
65 cells in response to antigenic stimulation<sup>1-4</sup>. In the context of antibody mediated immunity,  
66 B cells must migrate to the follicle where they (i) acquire and process antigen; (ii) present  
67 antigen to CD4<sup>+</sup> T helper cells; and (iii) organize into a germinal center (GC)<sup>5</sup>. Through the  
68 secretion of signaling molecules, fibroblastic reticular cells orchestrate both trafficking of B  
69 cells *to* and *within* different tissue sub-compartments, with dysregulation of migration leading  
70 to defective follicular homing<sup>6,7</sup>, aberrant follicular and GC organisation<sup>7,8</sup> and GC-derived  
71 lymphomas<sup>9</sup>.

72

73 Despite the importance of these migratory cues, the distances and scales over which they act  
74 are unclear. Many studies suggest that soluble factors, such as the cytokine IL-2, are spatially  
75 regulated through a diffusion-consumption mechanism that creates a concentration gradient  
76 capable of fine tuning cell behaviors through a graded exposure to ligand<sup>10</sup>. Consistent with  
77 the source-sink scheme of gradient formation atypical chemokine receptor 4-expressing  
78 lymphatic endothelial cells (LECs) lining the ceiling of the subscapular sinus have been  
79 implicated in the formation of functional CCL21 chemokine gradients in the lymph node<sup>11</sup>.  
80 Interestingly, both molecules are known to dynamically interact with extracellular matrix  
81 (ECM) components such as glycosaminoglycans (GAGs)<sup>12-15</sup>. Many soluble factors have  
82 carbohydrate-binding domains, a feature which may limit the capacity to undergo free  
83 diffusion, particularly in dense tissues<sup>12-14,16,17</sup>.

84

85 For many molecules, the ability to bind ECM components is a key determinant of  
86 functionality<sup>18,19</sup>. *In vivo*, truncation of the highly charged C-terminus of CCL21 prevents its  
87 immobilization to high endothelial venules (HEVs) while mutant forms of CC chemokines



88 that lack GAG-binding domains fail to induce chemotaxis into the peritoneum<sup>18,20</sup>. Mice  
89 carrying a mutated form of CXCL12 (CXCL12<sup>gagtm</sup>) where interactions with the ECM are  
90 impaired have disorganized germinal centers, as well as having fewer somatic mutations in  
91 immunoglobulin genes<sup>21</sup>. These experimental studies are supported by mathematical analyses  
92 predicting that gradient formation is increased when chemokines are secreted in matrix-  
93 binding form as compared to a non-matrix-interacting form<sup>22</sup>. This dichotomy has been  
94 explicitly studied in the context of CCL21, where immobilized and soluble gradients promote  
95 adhesive random migration or chemotactic steering of dendritic cells, respectively<sup>15</sup>.

96

97 In this study we focus on the chemokine CXCL13, a small globular protein with a theoretical  
98 average mass of 10.31 kDa that has emerged as a key regulator of B cell migration and  
99 lymphoid tissue architecture, with CXCL13<sup>-/-</sup> mice displaying aberrant follicular  
100 organization<sup>7,23,24</sup>. Similarly, mice deficient in CXCR5, the cognate receptor for CXCL13,  
101 have defective formation of primary follicles and GCs in the spleen, with B cells failing to  
102 home effectively to the follicles<sup>6,7</sup>. CXCL13 bioavailability is a dynamic function of  
103 production, diffusion, immobilization, mobilization, and consumption<sup>25</sup>. Consequently, the  
104 precise localization of CXCL13 within lymphoid tissues is difficult to visualize directly.

105

106 During selective ablation of follicular reticular cells, also known as follicular dendritic cells  
107 (FDCs), follicles remodel into disorganized bands of B cells that retain CXCL13-expressing  
108 stromal cell populations<sup>3</sup> suggesting that the cellular sources of this molecule are  
109 heterogeneous<sup>4</sup>. The expression patterns of CXCL13 also vary temporally over the course of  
110 immunization and infection. Expression is regulated in a positive feedback loop involving  
111 CXCR5-mediated induction of LT $\alpha_1\beta_2$  expression by B cells which in turn contributes to  
112 maximal CXCL13 production<sup>7</sup>. Once secreted, CXCL13 must diffuse through a dense  
113 environment comprising lymphocytes, reticular cells, vasculature, lymphatics and

114 extracellular matrix before undergoing internalization by typical and atypical chemokine  
115 receptors or protease-mediated enzymatic degradation<sup>11,26,27</sup>. CXCL13 has been shown  
116 experimentally to interact with heparan sulphate via two distinct binding interfaces<sup>17</sup>.  
117 Consistent with this structural study, recent single molecule imaging measurements of  
118 chemokine diffusion in *ex-vivo* murine tissue sections and collagen matrices suggest that  
119 chemokines may be heterogeneous in their mobility behaviors, with CXCL13 diffusion  
120 tightly constrained in tissues<sup>28</sup>. An additional layer of complexity is added by the  
121 heterogeneous distribution of ECM proteins within the follicle<sup>29</sup> and by altered chemotactic  
122 potency of many chemokines following proteolytic cleavage<sup>30,31</sup>. A number of proteases are  
123 known to alter chemokine activity including matrix metalloproteinases, dipeptidylpeptidase  
124 IV (CD26), aminopeptidase N (CD13), neutrophil granule proteases, and members of the  
125 cathepsin family<sup>30,31</sup>. However, the role of proteolytic processing in the context of gradient  
126 formation *in vivo* is poorly understood.

127

128 Given the complexity of the CXCL13 regulatory network, it is unclear if the molecule acts in  
129 an immobilized or soluble form and whether proteolytic processing is required to modulate  
130 CXCL13 function *in vivo*. This limited understanding is exacerbated by a dearth of  
131 experimental techniques capable of manipulating molecular gradients *in situ*. Our aim is to  
132 understand the mechanisms that create CXCL13 gradients within the B cell follicle. Here, we  
133 employ a modeling and simulation approach, mapping the reticular cell architecture of the  
134 primary follicle and reconstructing it *in silico*. We then apply a combination of machine  
135 learning and optimization approaches to systematically generate different chemotactic  
136 gradients and assess associated B cell scanning rates. Using this approach, it is possible to  
137 obtain insights where direct experimentation is intractable, generating data with high spatial  
138 and temporal sensitivity across multiple scales of organization.

139

140 Using a modelling and simulation approach, in combination with imaging and biochemistry,  
141 we assess the mechanisms that regulate CXCL13 gradient formation within lymphoid tissues.  
142 Our integrative approach shows that within the follicle, CXCL13 can exist in a soluble or  
143 immobile form. CXCL13 solubilization is regulated by the protease cathepsin B (*Ctsb*), with  
144 cleaved CXCL13 showing altered binding kinetics and increased chemotactic potency.  
145 Strikingly, in *Ctsb*-deficient mice B cell localization is highly variable, with an increased  
146 propensity to form ring-like structures around the T-cell zone, suggesting a key role for  
147 soluble CXCL13 in follicle formation. Our data thus suggest that reticular cells of the B cell  
148 zone generate microenvironments that shape both immobilized and soluble CXCL13  
149 gradients.

150

151

## RESULTS

### Mapping CXCL13<sup>+</sup> stromal cell networks in the B cell follicle

In this study we couple experimental and modeling approaches to identify and enumerate key entities and processes that regulate CXCL13 bioavailability (**Supplementary Figure 1**). To understand the cellular sources of CXCL13 within the primary follicle, we mapped the 3-dimensional (3D) organization of CXCL13<sup>+</sup> stromal cells in lymph node tissue sections from Cxcl13-Cre/TdTomato R26R-EYFP (abbreviated as Cxcl13-EYFP) mice<sup>4</sup>. In Cxcl13-EYFP mice EYFP acts as a lineage marker, endogenously expressed in cells that originate from a CXCL13-producing precursor, while TdTomato expression (red fluorescent protein, RFP) is confined to cells with current CXCL13 promoter activity. In addition, we identify FDCs as cells that are also CD21/35 positive (**Figure 1a**). From a follicle tissue cross-section, we mapped a network of  $198 \pm 39$  nodes and  $1163 \pm 242$  edges ( $n = 4$  mice), whereby we define nodes as the EYFP<sup>+</sup>RFP<sup>+</sup> reticular cells (RCs) and FDCs, while edges are indicated as physical connections between neighboring nodes (**Figure 1a, Supplementary Table 1**). We subdivide CXCL13<sup>+</sup> follicular reticular cells into two broad categories: CXCL13<sup>+</sup> CD21/35<sup>+</sup> FDCs and CXCL13<sup>+</sup> CD21/35<sup>-</sup> reticular cells (CD21<sup>-</sup> RCs) comprising reticular cells located underneath the subcapsular sinus (marginal reticular cells), and at the outer follicle. Interestingly, FDCs display significantly higher degree centralities and edge lengths than CD21<sup>-</sup> RCs, forming a dense sub-network within the follicle (**Figure 1b-c**). Topological analysis (as described in **Supplementary Note 1**) of the clustering coefficients ( $C_{\text{global}} = 0.57 \pm 0.02$ ,  $C_{\text{local}} = 0.60 \pm 0.02$ ) and the average shortest path length ( $4.17 \pm 0.26$ ) through the network has revealed a significant difference in the topological organization of the follicle network as opposed to an equivalent random network with the same number of nodes and edges ( $C_{\text{local}} = 0.06 \pm 0.01$ ,  $C_{\text{global}} = 0.06 \pm 0.01$  and shortest path length =  $2.41 \pm 0.11$ ). These results indicate that the follicle network exhibits small-world properties (**Figure 1d-e**) reminiscent of the T cell zone FRC network<sup>32</sup>. These findings are further corroborated by comparing the follicle network to an idealized small-world network (WS), demonstrating

179 their similarity in topological organization and small-world network metrics  $\sigma$  and  $\omega$   
180 (**Supplementary Table 1**). The small-world configuration is characterised by an  
181 overabundance of highly connected nodes, common connections mediating the short mean-  
182 path lengths. This property is associated with rapid information transfer and is also observed  
183 in airline routes and social networks<sup>33, 34</sup>. In the context of the follicle, this property is likely to  
184 promote complement mediated trafficking of antigen by non-cognate B cells from the  
185 subcapsular sinus to the FDC network, and also the migration of cognate B cells as they  
186 search for antigen within the follicle, and then present it to T-cells at the interfollicular border  
187 before seeding a germinal center reaction<sup>5,35,36</sup>.

188

#### 189 **Simulating and optimizing CXCL13 gradients *in silico***

190 Since the structural organization of CXCL13<sup>+</sup> reticular networks are a key determinant of  
191 follicle functionality, we hypothesized that that this cellular architecture may also regulate the  
192 molecular level patterning of CXCL13. To address this hypothesis, we use the stromal cell  
193 topology dataset to inform an algorithmic reconstruction of the follicular reticular cell  
194 network *in silico*<sup>37</sup>. Coupled with additional imaging datasets (**Supplementary Figure 1**), we  
195 engineered a high fidelity (**Supplementary Figure 3**) multiscale representation of the  
196 primary follicle in which immune cell agents can interact with reticular cells, creating and  
197 shaping complex physiological CXCL13 gradients (**Figure 2a, Supplementary Note 3**). This  
198 quantitative approach facilitates simulation analysis of CXCL13 gradient formation at very  
199 high spatiotemporal resolution but does require significant computational resources to  
200 evaluate (detailed in **Supplementary Note 2**); limiting the range of analysis techniques we  
201 can apply to understand CXCL13 gradient formation. To address this issue, we  
202 complemented our simulation analysis with an emulation-based approach (**Figure 2b,**  
203 **Supplementary Figure 2**). In this approach a machine-learning algorithm known as an  
204 artificial neural network (ANN) was used to learn the emergent behaviors of the simulator,  
205 such that it was capable of rapidly and accurately mapping between simulation inputs and

206 outputs averaged over a high number of replicate runs (**Figure 2b, Supplementary Figure**  
207 **2**).

208

209 To assess whether CXCL13 acts in principally an immobilized or a soluble form we focused  
210 on two potential models: Model 1 suggests that CXCL13 binds to extracellular matrix  
211 components creating short sharp gradients proximal to the CXCL13-secreting cells, while in  
212 Model 2 where CXCL13 is largely soluble and diffuses more freely throughout the tissue,  
213 creating a more homogeneous pattern (**Figure 2c**). To assess the veracity of each theory, a  
214 chemotactic landscape was created for each model through tuning parameters which control  
215 the rate of secretion, diffusion and decay but keep overall concentration fixed and the  
216 emergent scanning rates of *in silico* B cells were quantified under each scenario. This analysis  
217 predicted that Model 1 yields higher scanning rates than Model 2, suggesting that Model 1 is  
218 more likely (**Figure 2d**). To further assess the veracity of this result we perform an  
219 optimization analysis to determine the most effective spatial distribution of CXCL13 with  
220 respect to antigen scanning. In this analysis we employed the non-dominated sorting genetic  
221 algorithm-II (NSGA-II) <sup>38,39</sup> to systematically perturb parameters relating to CXCL13  
222 bioavailability *in silico* and determine a Pareto front of solutions (emergent cell migration  
223 behaviors) that represent the best trade-off obtained between fitting experimentally  
224 determined migration patterns (Objectives 1-3, detailed in Materials and Methods) <sup>40</sup> and  
225 maximizing scanning rates (Objective 4, detailed in Materials and Methods) <sup>40</sup>. Despite using  
226 a heuristic approach, performing this analysis on our multiscale simulator is computationally  
227 intensive due to: (i) a highly complex search space; (ii) the need for replicate runs to mitigate  
228 stochastic uncertainty; and (iii) multiple, conflicting objectives. To address this, we combined  
229 NSGA-II with our ANN-based emulator, an approach to determine the precise spatial  
230 distribution of CXCL13 that would not only fit our data, but also lead to optimal B cell  
231 scanning rates. This approach allowed us to examine the distributions of parameter values that  
232 give rise to our optimal solutions, such that we can mechanistically understand why some

233 spatial patterns are more effective than others. More specifically, we found that values of the  
234 CXCL13 diffusion constant are skewed towards low values, and decay rates skewed towards  
235 high values (**Figure 2e**), consistent with Model 1. In addition, we find that our objectives are  
236 conflicting, with increased scanning rates leading to poorer agreement between emergent cell  
237 behaviors *in silico* and laboratory measures (**Figure 2f**). Our theoretical analysis predicts that  
238 immobilized CXCL13 gradients are a key determinant of B cell trafficking patterns within the  
239 follicle.

240

#### 241 **CXCL13 forms immobilized gradients within the B-follicle**

242 To assess our theoretical prediction that CXCL13 can form immobilized gradients, we  
243 quantify binding of CXCL13<sup>AF647</sup> to tonsil tissue sections incubated with heparinase-II, an  
244 enzyme that cleaves both heparin and heparan sulphate or PBS (**Figure 3a**). By quantifying  
245 the fluorescent intensity for each image, we determine a significant drop in fluorescence  
246 intensity following heparinase-II treatment, suggesting that CXCL13 binds heparin and/or  
247 heparan sulphate in lymphoid tissue follicles (**Figure 3b**). To assess whether heparin and  
248 heparan sulphate constrain diffusion, we image CXCL13<sup>AF647</sup> diffusion within CD19<sup>+</sup> B cell  
249 follicles of tonsil tissue sections and quantify mobility with super-resolution precision at  
250  $\sim 500\text{Hz}^{41}$  (**Figure 3c**). Consistent with simulation analysis and immunohistochemistry we  
251 find that CXCL13<sup>AF647</sup> is largely immobile yielding a median [I.Q.R] diffusion rate of 0.19  
252  $[0.001\text{-}0.79] \mu\text{m}^2\text{s}^{-1}$ , while treatment with heparinase-II, led to increased rates of diffusion  
253 with a sample median [I.Q.R] diffusion coefficient of 1.6  $[0.47\text{-}3.9] \mu\text{m}^2\text{s}^{-1}$  ( $p < 0.0001$ )  
254 (**Figure 3c**).

255

256 Our super-resolution imaging assay permitted the tracking of single CXCL13 molecules,  
257 allowing us to characterize the heterogeneity of CXCL13 mobility *in situ*. Specifically, we  
258 identified and characterized distinct matrix bound (low-mobility) and soluble (high-mobility)

259 fractions (Figure 3d). Relative to the immobile fraction only a very small proportion of  
 260 CXCL13 was soluble, consistent with theoretical results. Disruption of the ECM through  
 261 heparinase-II treatment did lead to an increase in the mobile fraction. Given that such a large  
 262 proportion of CXCL13 was immobilized, we assessed whether we could detect an immobile  
 263 CXCL13 fraction within B cell follicles using immunohistochemistry in fixed human tonsil  
 264 and lymph node sections (**Figure 4a**). The spatial distribution of CXCL13 immunoreactivity  
 265 is spatially heterogeneous and strongly co-localized with the FDC marker CD35 (**Figure 4a**).  
 266 To quantify this observation, we measure the spatial autocorrelation of CXCL13 expression in  
 267 tonsil sections and determine the distance ( $D_{\text{uncorrelated}}$ ) at which there is no statistically  
 268 significant correlation in fluorescence intensities (**Figure 4b-c**). This analysis indicates that  
 269 CXCL13 expression is significantly correlated over short distances ( $\sim 50 \mu\text{m}$ ) before  
 270 becoming significantly uncorrelated with no statistically significant difference in  $D_{\text{uncorrelated}}$   
 271 between human tonsils and Model 1, corroborating our theoretical observation that CXCL13  
 272 can form complex immobilized gradients in the follicle (**Figure 4b-c**). This data shows that  
 273 CXCL13 interacts readily with extracellular matrix components, and together with stromal-  
 274 cell network architecture, shapes complex immobilized CXCL13 gradients within the B cell  
 275 follicle.

276

#### 277 **Cathepsin B generates soluble CXCL13 gradients**

278 Given the high affinity with which CXCL13 binds to the ECM, we hypothesized that it may  
 279 undergo proteolytic processing. In this study we focus on the cathepsin family; most  
 280 cathepsins identified in humans are lysosomal enzymes involved in metabolic protein  
 281 turnover but many cathepsins have also been reported to cleave chemokines<sup>30,31</sup>. In particular,  
 282 we have focused our attention on cathepsin B (Cath-B), which has been shown to regulate  
 283 cytokine expression during *L. major* infection<sup>42</sup>, is upregulated in many cancers<sup>43</sup>, and can be  
 284 produced in extracellular form in cytokine stimulated fibroblasts taken from rheumatoid  
 285 arthritis patients<sup>44</sup>.



286

287 Incubation of CXCL13 with Cath-B yielded two cleavage products with masses of 9.03 and  
288 8.68 kDa, respectively (**Figure 5a**). The smaller product is stable and forms across a range of  
289 enzyme substrate ratios in both humans and mice (**Supplementary Figure 4a**) and is detected  
290 at pH values between 4.0 and 7.2 with an optimal turnover rate between pH 5.0 and 6.5  
291 (**Supplementary Figure 4b**). Consistent with this data, single-molecule imaging of  
292 CXCL13<sup>[1-72]</sup> diffusion in 15% Ficoll showed a higher mobility rate for the Cath-B treated  
293 form of the molecule as compared to untreated ( $1.0 [0.04-3.6] \mu\text{m}^2\text{s}^{-1}$  and  $0.61 [0.08-2.2]$   
294  $\mu\text{m}^2\text{s}^{-1}$  respectively,  $p < 0.001$ ), indicating that the fluorescent tag incorporated into the C-  
295 terminus of the molecule had been cleaved (**Supplementary Figure 4c**).

296

297 To compare the heparin-binding capacity of CXCL13 and CXCL13<sup>[1-72]</sup> we loaded both  
298 peptides on a HiTrap heparin column followed by elution with an increasing concentration of  
299 NaCl. CXCL13<sup>[1-72]</sup> displays lower heparin-binding affinity and eluted at 0.53 M NaCl  
300 (**Figure 5b peak 2**) compared to intact CXCL13, which elutes at 0.62 M NaCl (**Figure 5b**  
301 **peak 3**). To assess if GAG-binding would protect CXCL13 from being proteolysed by Cath-  
302 B, we performed cleavage assays in the presence of different GAGs including hyaluronic  
303 acid, heparan sulfate and chondroitin sulfate. The presence of a 5- or 10-fold (w/w) excess of  
304 these GAGs, however, does not prevent CXCL13 processing by Cath-B (**Figure 5c**). In  
305 addition, we stained tonsil sections with an antibody against CXCL13 and quantify the total  
306 fluorescent intensity of each image following treatment with Cath-B or PBS (**Supplementary**  
307 **Figure 5**). Compared to PBS treatment, incubation with Cath-B led to a statistically  
308 significant reduction in the intensity of CXCL13 signal. In conclusion, GAGs do not affect  
309 Cath-B-mediated processing of CXCL13 *in situ*.

310

311 To assess the effect of C-terminal truncation of CXCL13 on cellular responses we compared  
312 CXCL13 and its cleavage product CXCL13<sup>[1-72]</sup> for their capacity to mobilize intracellular

313 calcium in CXCR5-transfected Pre-B 300-19 cells. Both CXCL13 and CXCL13<sup>[1-72]</sup> induce a  
314 rapid, transient intracellular calcium rise (**Figure 5d-e**). Analysis of internalization of CXCR5  
315 by flow cytometry show that CXCL13 and CXCL13<sup>[1-72]</sup> are equally potent inducers of  
316 internalization at concentrations of 100 and 300 nM (42.6 vs. 46.6% and 69.43 vs. 71.7%  
317 internalization, respectively) (**Figure 5f**). To determine if reduced binding of CXCL13<sup>[1-72]</sup> to  
318 heparin might also affect the chemoattractant activities for CXCR5<sup>+</sup> cells, we studied *in vitro*  
319 migration of primary B cells expressing endogenous CXCR5 (**Figure 5g**) and CXCR5-  
320 transfected Pre-B 300-19 (**Supplementary Figure 6**) cells to CXCL13 and CXCL13<sup>[1-72]</sup>. In  
321 both assays CXCL13<sup>[1-72]</sup> displays greater potency than full-length CXCL13; for primary B  
322 cells CXCL13<sup>[1-72]</sup> -induced migration at concentrations between 10 and 100 nM was  
323 significantly higher compared to full-length CXCL13 (**Figure 5g**). Consistent with the 2D  
324 migration assays, CXCL13<sup>[1-72]</sup> induces more potent chemotaxis of CXCR5-transfected Pre-B  
325 300-19 cells in a 3-dimensional matrigel at lower ligand concentrations (**Supplementary**  
326 **Figure 6b**).

327  
328 To determine if Cath-B was expressed in the follicle we performed IHC of tonsil tissue, with  
329 signal observed throughout the follicle, with highest expression co-localising with CD68<sup>+</sup>  
330 cells and some co-expression on CD35<sup>+</sup> stromal cells (**Figure 5h, 5i**). Analysis of the Cath-B  
331 expression in the human germinal center reaction indicates a higher abundance of Cath-B  
332 positive cells in the dark zone and CXCL13 producing stromal cells in the light zone. (**Figure**  
333 **5j**). This is corroborated through analysis of tonsil tissue lysates by western blotting  
334 (**Supplementary Figure 7**) and by data demonstrating that the *in vitro* culture medium of  
335 monocyte-derived macrophages is enzymatically active when assayed with the Cath-B  
336 specific substrate Z-Arg-Arg-AMC. A small discernable effect of innate stimuli (LPS) on  
337 Cath-B function was observed, the significance of which during immune responses remained  
338 unclear (**Supplementary Figure 7**).

339

340 To assess the *in vivo* importance of Cath-B in lymph node organisation and function we  
341 performed a detailed analysis of Cath-B (*Ctsb*) deficient mice. Relative to wild type, *Ctsb*<sup>-/-</sup>  
342 lymph nodes are often visibly smaller (**Figure 6a**) although there is no overall statistically  
343 significant decrease in the proportion of B cells in LNs (**Figure 6b**). To determine the role of  
344 Cath-B in B cell follicle formation staining of LNs were performed using antibodies specific  
345 for B cell markers (CD19, B220), T cells (CD4), LN HEVs (PNAd) and stromal-cell subsets  
346 (Podoplanin, CD21/35). Strikingly, we found the morphology of follicles in *Ctsb*<sup>-/-</sup> lymph  
347 nodes is highly variable relative to WT. In many instances, we observed that follicles are not  
348 always discrete, but rather form a thin rim of B cells continued along the SCS and in many  
349 instances we observe a ring like structure around the central T-cell zone (identified with  
350 immunoreactivity to CD4) (**Figure 6c**).

351  
352 This phenotype is suggestive of aberrant B cell homing and follicle formation, possibly  
353 through defects in HEV formation or function. However, we could find no statistically  
354 significant difference in total B cell numbers (**Supplementary Figure 11**) and using  
355 immunohistochemistry (Meca-79) we did not observe defects in the HEV network (**Figure**  
356 **6d**). Additionally, to determine if B cell homing is affected in *Ctsb* deficient mice, CFSE  
357 labelled CD45.1<sup>+</sup> B cells were transferred into either wild type or *Ctsb*<sup>-/-</sup> recipients. No  
358 difference is found in B cell homing into the LNs (**Figure 6e-g**). In addition, confocal  
359 microscopy of LN sections shows that while CFSE<sup>+</sup> cells clearly overlap with B220<sup>+</sup> areas of  
360 WT animals, CFSE<sup>+</sup> cells are much more disperse and are found more frequently in B220  
361 negative zones in *Ctsb*<sup>-/-</sup> mice. To corroborate these findings, we have performed RT-qPCR  
362 on whole LNs looking at a panel of genes relating to glycan synthesis and the formation of  
363 PNAd<sup>+</sup> HEV scaffolds (*Glycam1*, *Podxl*, *Cd34*, *Madcam1*, *Fcyl4*, *Fcyl7*), cellular adhesion  
364 (*Icam1*, *Vcam1*, *Pecam1*) and chemokines and their cognate receptors (*Cxcl13*, *Ccl19*, *Cxcr5*,  
365 *Ccr7*). With the exception of *Podxl*, we find no statistically significant difference in deltaCT  
366 values for each gene when comparing WT and *Ctsb*<sup>-/-</sup> mice (**Figure 6h and Supplementary**  
367 **Figure 8**). A small but non-significant decrease in CXCL13 and CXCR5 was observed likely

368 reflecting a failure in FDC network formation (**Figure 6g**). These datasets suggest that  
369 CXCL13 can be solubilized by Cath-B, and that soluble CXCL13 gradients are essential for  
370 the formation of primary follicles within the LN. Taken in concert our data suggests that  
371 CXCL13 can exist in both immobilized and soluble forms, with availability fine-tuned by the  
372 reticular-cell microenvironment, and by the enzyme Cath-B.  
373

374 **DISCUSSION**

375 Soluble factors are an essential means of communication between cells and their environment.  
376 In the context of the immune system this cross-talk ensures that each B cell receives the  
377 appropriate signal at the appropriate time <sup>5,45</sup>. However, there is currently a lack of a well-  
378 accepted model to describe the spatial distribution of soluble factors *in situ*<sup>25</sup>. The data  
379 presented in this study highlights the importance of the tissue microenvironment in shaping  
380 gradients and raises the question of whether assuming free diffusion can provide sufficiently  
381 accurate theoretical models capable of generating novel predictions.

382  
383 Using a modeling and simulation approach we show that there is an underlying regulation to  
384 the spatial organization of CXCL13 at the cellular level, identifying a small-world network  
385 topology with regions of high connectivity and long-range connections between these cliques.  
386 These guidance structures are likely to promote trafficking of cognate B cells within the  
387 different niches of the B cell microenvironment and the CR2-mediated delivery of large  
388 antigen from the subcapsular sinus to the B cell zone reticular cell network by non-cognate B  
389 cells. Our data thus provides a unique insight into how the primary follicle is structurally  
390 organized to promote B cell homeostasis and activation. We posit that the distinct topological  
391 properties of the reticular cell network with dense connectivity between cells are likely to  
392 create a labyrinth of single-cell niches, within which B cells scan for antigen. In future studies  
393 it would be of interest to assess whether the small-world properties of stromal cells in the  
394 primary follicle are maintained in the secondary follicle with a formed germinal center.

395  
396 The implications of this cellular architecture also manifest at the molecular scale. By utilizing  
397 modeling and simulations in conjunction with imaging approaches, we propose a model  
398 whereby CXCL13 is largely immobile, with diffusion constrained by the localized tissue  
399 microenvironment. While our results indicate that heparin and heparan sulphate are important  
400 factors regulating the spatial distribution of CXCL13 it would also be of interest to know if

401 other ECM components found in the follicle also contribute to CXCL13 immobilization.  
402 Importantly, our data suggests that immobilized CXCL13 is likely to form complex  
403 landscapes within tissues – a conceptual change in our understanding of the form that  
404 gradients may take *in vivo*. Results from our multi-objective optimization emulation  
405 experiments suggest that this spatial profile is functionally important, promoting higher rates  
406 of scanning than homogeneous landscapes. This data is consistent with previous studies  
407 highlighting the importance of ECM components in modulating immune cell recruitment  
408 <sup>15,18,21</sup>.

409  
410 Interpretation of immobilised gradients may require proteolytic processing by Cath-B,  
411 yielding a truncated molecule capable of binding and signalling through CXCR5 but  
412 displaying reduced affinity for the ECM. Importantly, low concentrations of CXCL13<sup>[1-72]</sup>  
413 were more potent than intact CXCL13 in attracting CXCR5 transfected Pre-B cells or primary  
414 B cells. Until recently, Cath-B in immune cells was regarded as a lysosomal enzyme  
415 responsible for protein degradation, although cell membrane bound Cath-B has been shown to  
416 be functional in immune cells and can function across a range of pH values<sup>46,47</sup>. Our findings  
417 suggest extracellular occurrence and active secretion from both macrophages and reticular  
418 cells. Given that Cath-B activity is most potent at low pH values, and inflammation can lead  
419 to a decrease in tissue pH it was interesting to note the increased secretion of Cath-B in the  
420 presence of LPS. However, it is unclear if this is an active release mechanism that occurs *in*  
421 *vivo*. It is possible that the initial influx of antigen triggers increased availability of CXCL13  
422 at the subcapsular sinus, where antigen-presenting macrophages can then recruit both cognate  
423 B cells and non-cognate B cells to facilitate GC seeding and antigen deposition on the B cell  
424 zone reticular cell network. Strikingly, follicular architecture in *Ctsb*-deficient mice bears a  
425 strong resemblance to the phenotype observed in lymphoid tissues of CXCL13 deficient  
426 mice<sup>7</sup>, and in the spleens of CXCR5 deficient mice<sup>6</sup>. This is consistent with a model where

427 soluble CXCL13 drives chemotactic homing behaviours while immobilized CXCL13  
428 promotes haptokinetic scanning within the follicle, as has been demonstrated for CCL21<sup>15</sup>. In  
429 future studies it would be interesting to assess the validity of this model and to assess whether  
430 perturbing Cath-B mediated regulation of CXCL13 *in vivo* can alter the onset and efficacy of  
431 affinity maturation, and whether other enzymes are involved in CXCL13 processing.

432 Engineering approaches often draw inspiration from natural systems to solve complex design  
433 problems; however, they can reciprocally influence our understanding of the immune system,  
434 providing a quantitative framework from which to understand the spatial distribution of  
435 morphogens. Using an ensemble of different techniques, we were able to consolidate several  
436 disparate datasets and through simulation-based experimentation have generated insights that  
437 informed subsequent experimental work. Specifically, we have highlighted the use of data-  
438 driven machine learning and evolutionary computational approaches to expedite the  
439 translation of simulator-derived insights into a better understanding of the design,  
440 organization, dynamics, and function of complex biological systems.

441

442 In conclusion, our data suggests that CXCL13 can exist in both immobilized and soluble  
443 forms, with the precise mode of availability dependent on enzymatic processing by Cathepsin  
444 B. This provides a significant update in our conceptual understanding of how homeostatic  
445 chemotactic gradients arise and form functional gradients in complex tissues.

446  
447

448 **METHODS**

449 **Enzymatic treatment of tonsil sections:** Frozen lymph node or tonsil sections on polylysine  
450 slides were incubated at room temperature for 30 mins. A circle was drawn around each  
451 section using a wax ImmEdge pen (Vector Laboratories), the sections were then hydrated  
452 with PBS for 5 mins and incubated with 150nM recombinant Cath-B (Sigma-Aldrich) for 3  
453 hrs at 37°C or with 10U heparinase II (Sigma-Aldrich) for 1 h at 17°C. Slides were washed in  
454 PBS and then processed for immunohistochemistry (as described below) with no fixative. All  
455 samples were ethically approved and informed consent was obtained from all participants.  
456 Tonsils were collected under NRES REC 12/NE/0360 approved study (IRAS: 114771) to  
457 MCC. Hepatic lymph nodes were collected during multi-organ donation procedures, after  
458 approval by the Medical Ethical committee of the Erasmus MC (MEC-2014-060) by WGP.

459

460 **Immunohistochemistry and immunofluorescence:** Frozen lymph node or tonsil sections on  
461 polylysine slides were incubated at room temperature for 30 mins, fixed in acetone or 4%  
462 PFA and then washed in PBS for 15 mins in total with changes of PBS every 5 mins. Sections  
463 were incubated in a blocking buffer of PBS and 5% serum (the serum of the host the  
464 secondary antibody was raised in) at room temperature for 1hr at room temperature. After  
465 blocking, sections were incubated in the primary antibody mix, made up in blocking buffer  
466 for 1hr at RT. The slides were then washed, and secondary antibody incubation was  
467 performed (if necessary). For experiments where exogenous CXCL13<sup>AF647</sup> was used to  
468 measure binding to tissue, incubation of unfixed tissue sections with 500nM CXCL13<sup>AF647</sup> for  
469 1 hour at RT instead of the secondary antibody-staining step. Samples were washed 5 mins in  
470 PBS. A drop of Prolong gold (Invitrogen) was added to each section, and then a No 1.5 glass  
471 coverslip (Fisher) mounted on top. The slides were incubated overnight at 4°C the next day  
472 slides were sealed using nail varnish and stored at 4°C. Immunofluorescent stained sections  
473 were imaged using the Zeiss LSM 880 confocal microscope. Samples were excited with  
474 405,488,561 and 633 nm lasers. Image acquisition was performed using the 63X oil objective.



475 Tile scans and Z stacks were performed to image large tissue sections at high-resolution. For  
476 imaging of chemokine gradients, we used the Airyscan module to increase spatial resolution  
477 beyond the diffraction limit of light. A list of commercial antibodies used in this study are  
478 available in **Supplementary Table 2**.

479

480 For immunohistochemistry on human tonsil sections, specimens were fixed in 10% buffered  
481 formalin, embedded in paraffin and cut into 4µm cross-sections for immunostaining.  
482 Deparaffinized and rehydrated sections were boiled at 95C for 30 mins in target retrieval  
483 solution (S1699 DAKO) and then treated with peroxidase blocking reagent (S2001, DAKO)  
484 when needed, and protein block serum-free (X0909, DAKO). Sections were incubated  
485 overnight at room temperature with anti-CD3 at 5ug/ml, anti-Cath-B at 0.12ug/ml and anti-  
486 CXCL13 at 1ug/ml. Next biotinylated anti-mouse IgG, anti-rabbit IgG, or anti-goat IgG were  
487 used at 2 µg/ml and applied for 30 minutes at room temperature. Slides were washed  
488 and incubated with StreptABComplex (K0377, K0391, DAKO). Double-staining for  
489 CD3 and Cath-B was performed in two steps; slides were blocked with 3 µg/ml rabbit  
490 IgG (X0936, DAKO) after incubation with anti-CD3. For CXCL13 single staining in  
491 immunohistochemistry, after anti-CXCL13 antibody, sections were incubated with  
492 MACH1 with primary antibodies, the sections were incubated with corresponding  
493 secondary antibodies manufacturer's instructions. Sections were developed with  
494 either DAB or New Fuchsin and nuclei counterstained with hematoxylin. For  
495 immunofluorescence stainings; after incubation with primary antibodies, the sections  
496 were incubated with corresponding secondary antibodies from Alexa for 30 minutes  
497 and then nuclei counterstained with DAPI.

498

499 Mouse lymph node frozen sections (8µm) from Ctsb<sup>-/-</sup> and controls were hydrated and  
500 washed using PBS; each wash step was 5 min, repeated three times. Sections were  
501 incubated in blocking buffer (PBS 5% goat serum) at room temperature for 5 min.  
502 Following blocking sections were incubated in a primary antibody staining mix, made  
503 up in blocking buffer, for 1 hour at room temp. Slides were washed, then incubated in  
504 secondary antibody staining mix, made up in blocking buffer, for 1 hour at room  
505 temp. Following a final wash ProLong Gold (Invitrogen) was added to each section,  
506 then a No 1.5 glass coverslip mounted, slides were incubated overnight at 4°C and  
507 sealed with nail varnish. The antibodies used in staining mixes were; MECA-79  
508 Alexa488 (Nanotools (Custom Product), 1 in 200 dilution); PDPN Alexa 594  
509 (Biolegend (8.1.1)(Cat. 127414); B220 Alexa488 (Biolegend (RA-6B2)(Cat. 103225),  
510 1 in 200 dilution); CD4 Alexa647 (Biolegend (RM4-5)(Cat. 100516), 1 in 200  
511 dilution); CD21/35 Alexa647 (Biolegend (7E9)(Cat. 123424) 1 in 200 dilution); and  
512 CD19 Alexa 647 (Biolegend (6D5)(Cat. 11512), 1 in 200 dilution). All experiments  
513 involving mice conformed to the ethical principles and guidelines approved by the  
514 University of York Institutional and Animal Care Use Committee in accordance with  
515 the European Union regulations and performed under a United-Kingdom Home  
516 Office License.

517

518 **Reticular cell topology:** Topological analysis was performed using the methodology as  
519 previously described<sup>48</sup>. 3D images (approx. 450µm x 450µm x 35µm) of lymph nodes from  
520 Cxcl13-EYFP mice were obtained by laser scanning confocal microscopy. Experiments were  
521 performed in accordance with federal and cantonal guidelines (Tierschutzgesetz) under  
522 permission numbers SG10/16, SG07/16 and SG05/15 following review and approval by the  
523 Cantonal Veterinary Office (St. Gallen, Switzerland). The topological mapping of follicular

524 stromal cell network structure was created as an undirected unweighted graph by defining  
525 nodes as the EYFP<sup>+</sup>RFP<sup>+</sup> follicular stromal cells and edges as physical connections between  
526 neighboring nodes. The network edges in 3D Z-stack images were annotated using the  
527 Measuring Tool in Imaris (Bitplane) such that a straight line is demarcated between adjacent  
528 stromal cells that are connected by a cellular protrusion or smaller branching process with no  
529 other cell body directly blocking this connection. Analysis of key topological parameters  
530 (described in **supplementary table 1**) was performed using the iGraph package in R. These  
531 parameters enable the assessment whether the network has small-world properties as has been  
532 reported for T cell zone FRC networks in lymph nodes <sup>32</sup>. Although many additional  
533 topological and structural metrics exist, the metrics proposed in this study are sufficient to  
534 perform a basic characterisation of the follicle network, while also providing quantitative data  
535 to inform the algorithmic reconstruction of an *in silico* stromal network model.

536

537 **Quantifying the spatial autocorrelation of fluorescence:** To quantify the spatial  
538 autocorrelation of fluorescence intensity 2D confocal images were acquired on a Zeiss LSM  
539 880 confocal microscope with the same laser settings and post processing for each sample.  
540 Processed .png files were then analyzed in R using custom scripts. Briefly, this analysis  
541 involved discretizing the image into 14.44  $\mu\text{m}^2$  bins and calculating the spatial correlogram  
542 using the correlog function from the ncf package. Spatial autocorrelation is quantified using  
543 Moran's I statistic with significance assessed through permutation testing <sup>49,50</sup>.

544

545 **Super-resolution imaging:** Frozen tonsils sections on polylysine slides were incubated at  
546 room temperature for 30 minutes. Samples were hydrated in PBS for 5 mins then left to dry  
547 and circles were drawn around each section with a wax ImmEdge pen (Vector Laboratories).  
548 Sections were incubated in a blocking buffer of PBS + 5% goat serum (Sigma) at room  
549 temperature for 1 hour. After blocking, sections were incubated in primary antibody mix  
550 (anti-B220 FITC, eBioscience) made up in 1:200 blocking buffer for 1 hour at room

551 temperature. Samples were washed with PBS for  $3 \times 5$  minutes and 30 nM of CXCL13-AF-  
 552 647 were added to the slides. Slides were left to incubate overnight at 4°C after which slides  
 553 were washed for 30 seconds in PBS and a No. 1.5 glass coverslip (Fisher) mounted on top.

554 Bespoke fluorescence microscopy was performed on an inverted microscope (Nikon Eclipse  
 555 Ti-S) with a 100× NA 1.49 Nikon oil immersion lens and illumination from a supercontinuum  
 556 laser (Fianium SC-400-6, Fianium Ltd.), controlled with an acousto-optical tunable filter  
 557 (AOTF) to produce a narrowfield excitation light centred on 619 nm<sup>51,52</sup>. The use of  
 558 narrowfield imaging permits fluorescent excitation at distance of a few hundred nanometers  
 559 above the coverslip thus mitigating some of the boundary effects which may be encountered  
 560 using Total Internal Fluorescence (TIRF) microscopy where only a thin section directly above  
 561 the coverslip is excited<sup>53</sup>. A 633 nm dichroic mirror and 647 nm long-pass emission filter  
 562 were used to filter the appropriate wavelengths of light emitted from the fluorescence images.

563 Images were recorded on an emCCD camera (860 iXon<sup>+</sup>, Andor Technology Ltd) cooled to -  
 564 80°C. 128×128 pixel images were acquired for 1000 frames with 1.98 ms exposure times.  
 565 The camera was in frame transfer mode with the resulting frame rate being 513 Hz. The  
 566 electron-multiplier gain was set to 300. The kinetic series were saved as TIFF format files  
 567 (.tiff). When imaging in tissue, sections were stained with an anti-B220 (1 in 200 dilution)  
 568 antibody conjugated to FITC. Samples were imaged at low (1.2 µm/pixel) magnification with  
 569 green illumination (470 nm) to determine the location of the B cell follicles, before switching  
 570 to high (120 nm/pixel) magnification and red illumination to image chemokines in these  
 571 areas.

572

573 The analysis of the kinetic series was done in bespoke Matlab software, namely ADEMS  
 574 code<sup>52</sup>, which enabled objective single molecule detection and tracking to within 40 nm  
 575 spatial precision, utilizing a combination of iterative Gaussian masking and local  
 576 background subtraction to calculate sub-pixel precise estimates for the intensity centroid  
 577 of each candidate fluorescent dye in the image with edge-preserving filtration of intensity

578 data and Fourier spectral analysis to confirm detection of single dye molecules<sup>54-57</sup>. The  
579 code was first performed on simulated kinetic series that mimicked the signal and noise  
580 landscape of real image data. The parameter settings such as values for the signal-to-noise  
581 ratio and the Gaussian mask size of ADEMS code were set so that the code accurately  
582 identified the signals in the simulated data. These parameters were then used in the code  
583 for the identification of single fluorescent signals in real data. From these fluorescent  
584 spots ADEMS code then produced trajectories of fluorophores that last five or more  
585 consecutive frames to allow the calculation of microscopic diffusion coefficients as the  
586 gradient of a linear fit to the first four positions in each track<sup>58,59</sup>. These coefficients were  
587 plotted in histograms with integer bin sizes for easy comparison between the experiment  
588 and the control groups.

589

590 **Emulator development:** As an agent based model a number of high-level properties emerge  
591 from the simulator due to aggregated interactions between agents and their environment<sup>60,61</sup>.  
592 To learn the complex relationship between parameter inputs and emergent agent behaviours  
593 we employ a supervised machine learning approach. Supervised learning involves generating  
594 a dataset of inputs ( $x$ ) and outputs ( $y$ ) and then teaching an algorithm to approximate a  
595 mapping function between the two. With a sufficiently accurate mapping function it is then  
596 possible to predict  $y$  for a set of unobserved values of  $x$ .

597

598 The training dataset for emulator development was obtained using Latin hypercube  
599 sampling<sup>62</sup>, with 3000 parameter sets. Each set was executed 100 times to mitigate aleatory  
600 uncertainty, and median responses calculated to summarize simulator performance under  
601 those conditions.

602

603 To map the complex relationship between parameter inputs and the emergent properties of the  
604 model we train an artificial neural network (ANN) using the SPARTAN<sup>63</sup> package in R.  
605 ANNs are a technique inspired by the neuronal circuits in the brain, with computations  
606 structured in terms of an interconnected group of artificial neurons organised in layers. In this  
607 scheme parameter inputs are passed into the network and iteratively processed by a number of  
608 hidden layers. Within each hidden layer the sum of products of inputs and their corresponding  
609 weights are passed through a sigmoidal activation function that is fed as inputs into the next  
610 layer. This process is repeated until the output layer is reached and we have a prediction for  
611 the output values. During the learning phase, the weighting of connections between neurons is  
612 adjusted in such a way that the network can convert a set of inputs (simulation parameters)  
613 into a set of desired outputs (simulation responses) <sup>64</sup>.

614

615 A key technical consideration when developing neural networks is how to evaluate predictive  
616 power. Testing predictive performance on the training data is not useful as it can lead to over  
617 fitting, whereby the network is poor at predicting previously unobserved data. To solve this  
618 problem, a proportion of the dataset is omitted from the training dataset and used to validate  
619 algorithm performance. To evaluate the predictive power of the emulator we partition the  
620 LHC dataset into training (75%), testing (15%) and validation (10%) datasets. Partitioning the  
621 data incurs a cost however, as we reduce the number of samples used for training the model.  
622 In addition, the data used to train the model, even if not used in the evaluation process, can  
623 have a significant impact on predictive performance. To address these issues, we perform a  
624 procedure known as k-folds cross validation. In this scheme the data is partitioned into k-folds  
625 and the algorithm learns the mapping between inputs and outputs using k-1 folds as training  
626 data with validation performed on the remaining part of the data. This process is repeated  
627 until each fold is used as the test set with overall performance taking as the average for each  
628 fold. To develop our ANN, we generate multiple neural network structures with different  
629 number of hidden layers and nodes within each layer (so called hyperparameters) but fixed

input and output layers (one node for each distinct input and output respectively. The accuracy of each putative network was quantified using the root mean squared error between the predicted cell behavior responses and those obtained by the simulator. Using this approach an ANN was developed for each simulation output metric with network structures presented in **Supplementary Figure 9**.

**Multi-objective optimization:** Multi-objective optimization analysis was performed using the non-dominated sorting genetic algorithm II (NSGA-II), a multiobjective genetic algorithm<sup>39</sup>. This analysis was performed in R using the package mco v15.0. The four objectives to be optimised by the algorithm were to: minimize the root mean squared error between emulator and simulator responses for cell speed, meandering index and motility coefficient; and maximize scanning rates.

**Preparation of recombinant Cxcl13:** Preparation of recombinant CXCL13, full length and 1-72 form was prepared as described previously<sup>65</sup>. CXCL13 labeled with the fluorescent tag AF647 was purchased from Almac.

**CXCL13-processing by Cath-B:** Synthetic human or mouse CXCL13<sup>66</sup> was incubated with purified human liver Cath-B (Athens) (For mice CXCL13 was incubated with recombinant Cath-B purchased from R&D systems) at 37°C in Dulbecco's PBS (DPBS, Invitrogen) pH 6.8 containing 4 mM EDTA and 2 mM L-cysteine. The reaction was stopped by boiling the samples at 95°C for 5 mins. The chemokine cleavage products were separated by Tris-Tricine SDS-PAGE and stained with Coomassie blue. Enzymes were activated as per the manufacturer's instructions.

**Interaction of CXCL13 with glycosaminoglycans:** CXCL13 and CXCL13<sup>[1-72]</sup> binding to heparin was characterized by loading respective chemokine samples on a 1 ml Hitrap<sup>TM</sup>

657 heparin column (GE Healthcare). Bound CXCL13 and CXCL13<sup>[1-72]</sup> were eluted using a  
658 linear gradient of 0 to 1.0 M NaCl in 10 mM potassium phosphate, pH 7.5 over 30 mins at a  
659 flow rate of 1 ml/min and monitored by absorbance at 280nm on a DuoFlow system (Bio-  
660 Rad). The impact of soluble glycosaminoglycans on CXCL13 processing by Cath-B was  
661 determined by performing CXCL13 cleavage experiments in the presence of hyaluronic acid,  
662 heparan sulfate or chondroitin sulfate (Sigma).

663

664 **Intracellular calcium mobilization:** CXCL13-induced changes in cytosolic free  $\text{Ca}^{2+}$ -  
665 concentration  $[\text{Ca}^{2+}]_i$  were measured in CXCR5-transfected mouse Pre-B 300-19 cells<sup>24</sup>. Cells  
666 were loaded with 0.2 nmol of fura 2-AM per  $10^6$  cells for 20 min at 37°C in a buffer  
667 containing 136 mM NaCl, 4.8 mM KCl, 1 mM  $\text{CaCl}_2$ , 1 mg/ml glucose and 20 mM Hepes,  
668 pH 7.4 (MSB). After centrifugation, fura-2 loaded cells were resuspended in MSB, stimulated  
669 at 37°C with the indicated concentrations of intact or truncated CXCL13, and the  $[\text{Ca}^{2+}]_i$   
670 related fluorescence changes were recorded as previously described<sup>67</sup> Relative units are  
671 calculated as the ratio of the fluorescence signal after chemokine stimulation and a calibration  
672 signal.

673

674 **CXCR5 internalization:**  $3 \times 10^5$  CXCR5-transfected Pre-B 300-19 cells were washed with  
675 DPBS and incubated for 45 min at 37°C or 4°C (control) in 50  $\mu\text{l}$  DPBS containing 2% PPL  
676 (human albumin, CSL Behring) and the indicated concentrations of intact or truncated  
677 CXCL13. Cells were then washed with ice cold DPBS supplemented with 1% BSA (fraction  
678 V, Applichem) and 0.04% sodium azide and blocked with 3 mg/ml Vivaglobulin (CSL  
679 Behring) for 12 min at 4°C before incubation with anti-human CXCR5 antibody (1:40) or  
680 isotype control (1:40). Surface receptor expression was evaluated by flow cytometry.

681



682 **Cell migration:** 2-dimensional chemotaxis assays with human B cells and CXCR5-  
683 transfected Pre-B 300-19 cells were carried out in 5- $\mu$ m pore size Transwell plates (Costar).  
684 Cells were washed and resuspended at  $5 \times 10^6$  cells/ml in RPMI containing 10% FBS  
685 (Invitrogen), L-glutamate, sodium pyruvate and 2-mercaptoethanol. Chemokines were diluted  
686 in the same buffer and added to the wells. Filter inserts were then placed in the wells and the  
687 assay was started by adding 100  $\mu$ l of cell suspension into the filter inserts. After 2 h at 37°C  
688 and 5% CO<sub>2</sub>, the filter inserts were removed, and the migrated cells counted by flow  
689 cytometry (FACSCalibur Becton Dickinson) for 30sec using a high flow preset. Assays were  
690 carried out in duplicates and tests from different days were standardized by measuring PKH26  
691 reference microbeads (Sigma) under the same conditions. Cell migration in a 3D setup was  
692 assessed as described previously<sup>68,69</sup>. Briefly,  $5 \times 10^4$  CXCR5 transfected pre-B 300-19 cells  
693 in 100  $\mu$ l RPMI 1640 medium supplemented with 10% fetal calve serum and 0.1%  $\beta$ -  
694 mercaptoethanol were pre-mixed at 4°C with growth-factor reduced Matrigel (Corning, BD  
695 Biosciences #356231) to a final Matrigel concentration of 300  $\mu$ g/ml and seeded to the upper  
696 well of a 24-well Transwell™ System and polycarbonate filters with a pore size of 5  $\mu$ m  
697 (Corning Costar). Matrix was allowed to polymerize for 2h at 37°C/5% CO<sub>2</sub>. Cells were  
698 subsequently allowed to migrate through the Matrix for 3.5h towards the lower well  
699 containing graded concentrations of the chemokines. The numbers of input and migrated cells  
700 were determined by flow cytometry (LSRII, BD Biosciences).

701

702 **Quantifying lymph node cellularity:** Accucheck counting (Invitrogen) beads were used to  
703 calculate total cellularity of murine popliteal lymph nodes. Following antibody staining,  
704 pellets were resuspended in 100 $\mu$ l FACs wash. 100 $\mu$ l of counting beads were mixed for 1 min  
705 to ensure they were evenly resuspended before running on the flow cytometer. To ensure  
706 accuracy the beads are made up of two types of beads that differ in their fluorescent intensity,  
707 for accurate readings the two populations should be present at approximately 50:50 ratio. To  
708 calculate absolute cell number. The following calculation was then made:

$$\text{Number of cells per } \mu\text{l} = \frac{\text{number of events(beads)}}{\text{number of events}} \times \text{number of beads per } \mu\text{l}$$

709 Where the number of beads per  $\mu\text{l}$  was provided by the supplier and varied with each batch.  
 710 The total cellularity of the lymph node could be calculated using the values of cells per  $\mu\text{l}$  and  
 711 final volume of FACS wash that contained the cells.

712

713 **Real-time Quantitative PCR:** RNA was extracted from whole LNs using RLT buffer  
 714 (Qiagen), the lysates were stored at  $-20^{\circ}\text{C}$  overnight. RNA extraction was performed using an  
 715 RNeasy mini kit (Qiagen). Quantity and quality of RNA was measured using a NanoDrop  
 716 spectrophotometer. Samples were stored at  $-80^{\circ}\text{C}$ . cDNA synthesis was performed using the  
 717 High Capacity cDNA Reverse Transcription Kit (Applied Biosystems) and a thermo cycler  
 718 PCR machine. cDNA samples were stored at  $-20^{\circ}\text{C}$ . The following Taqman probes  
 719 (ThermoFisher cat. 4331182) were utilized: CCL19 (Mm00839966\_g1); CXCL13  
 720 (Mm04214185\_s1); GlyCAM-1 (Mm00801716\_m1); Podxl (Mm00449829\_m1); CD34  
 721 (Mm00519283\_m1); MADCAM (Mm00522088\_m1); FucT IV (Mm00487448\_s1); FucT  
 722 VII (Mm04242850\_m1); VCAM (Mm01320970\_m1); PECAM (Mm01242576\_m1); ICAM  
 723 (Mm00516023); CXCR5 (Mm00432086\_m1); CCR7 (Mm99999130\_s1).

724

725 **B cell *in vivo* homing assays:** B220<sup>+</sup> B cells were isolated from CD45.1 congenic mice; and  
 726 stained with anti-B220, sorted on a S3 BioRad cell sorter and labelled with CFSE for 10min  
 727 in serum free medium. Labelled cells were washed in complete medium prior to resuspension  
 728 in PBS,  $10^7$  B220<sup>+</sup> CFSE labelled were transferred intravenous into either Ctsb<sup>-/-</sup> or wildtype  
 729 recipients. Twenty-four hours post transfer, LNs were isolated and 8mm frozen sections cut.  
 730 Sections were counter stained with anti-B220 Alexa647 (Biolegend) and imaged on a Zeiss  
 731 810 confocal microscope. Experiments were performed in accordance with federal and  
 732 cantonal guidelines (Tierschutzgesetz) under permission numbers SG10/16, SG07/16 and  
 733 SG05/15 following review and approval by the Cantonal Veterinary Office (St. Gallen,  
 734 Switzerland). To determine the relative efficiency of WT vs Ctsb<sup>-/-</sup> B cells to enter into WT or

735 Ctsb<sup>-/-</sup> recipient mice equal numbers of CFSE (ThermoFisher) labelled KO cells and CMTMR  
736 (ThermoFisher) labelled WT cells were transferred into corresponding recipient mice. The  
737 absolute number of B cells was determined by multiplying absolute cell counts from  
738 individual matched inguinal LNs using (CASY) with flow cytometry analysis of isolate  
739 lymphocytes with CD19-APC (Biolegend) and CD3eBrilliantViolet (Biolegend) on a  
740 FortessaX20 (BD). The ratio of transferred B (B220+) cells KO:WT was calculated in both  
741 LN and spleen of the different recipient mice taking into account the relative efficiency of  
742 CFSE and CMTMR labelled survival post transfer by calculating the ratio of WT CFSE:WT  
743 CMTMR transferred cells (Cell number x % B cells of CFSE<sup>+</sup> or CMTMR<sup>+</sup> populations). The  
744 gating strategy for flow cytometry analysis is shown in **Supplementary Figure 12**. This  
745 methodology removed the effect of CMTMR non-specifically affecting the efficiency of dye  
746 labelled lymphocyte survival post transfer.

747

#### 748 **Code Availability:**

749 A brief overview of the simulator platform is presented in **supplementary note 3**. A full  
750 description of model simulator design, development and validation, as well as associated  
751 source code, is available from  
752 <https://www.kennedy.ox.ac.uk/technologies/resources/cxcl13sim>

753

754 **Data Availability:** Source Data is provided in Zip folder. All Raw datasets (1.5GB zip file)  
755 that support the findings of this study are available from the corresponding author upon  
756 reasonable request.

757

## 758 1. REFERENCES

- 759 1. Junt, T., Scandella, E. & Ludewig, B. Form follows function: lymphoid tissue microarchitecture in  
760 antimicrobial immune defence. *Nat. Rev. Immunol.* **8**, 764–775 (2008).
- 761 2. Link, A. *et al.* Fibroblastic reticular cells in lymph nodes regulate the homeostasis of naive T cells. *Nat.*  
762 *Immunol.* **8**, 1255–1265 (2007).
- 763 3. Wang, X. *et al.* Follicular dendritic cells help establish follicle identity and promote B cell retention in  
764 germinal centers. *J. Exp. Med.* **208**, 2497–2510 (2011).
- 765 4. Onder, L. *et al.* Lymphatic Endothelial Cells Control Initiation of Lymph Node Organogenesis. *Immunity* **47**,  
766 80-92.e4 (2017).
- 767 5. Pereira, J. P., Kelly, L. M. & Cyster, J. G. Finding the right niche: B cell migration in the early phases of T-  
768 dependent antibody responses. *Int. Immunol.* **22**, 413–419 (2010).
- 769 6. Förster, R. *et al.* A Putative Chemokine Receptor, BLR1, Directs B Cell Migration to Defined Lymphoid  
770 Organs and Specific Anatomic Compartments of the Spleen. *Cell* **87**, 1037–1047 (1996).
- 771 7. Ansel, K. M. *et al.* A chemokine-driven positive feedback loop organizes lymphoid follicles. *Nature* **406**,  
772 309–314 (2000).
- 773 8. Allen, C. D. C. *et al.* Germinal center dark and light zone organization is mediated by CXCR4 and CXCR5.  
774 *Nat. Immunol.* **5**, 943–952 (2004).
- 775 9. Muppidi, J. R. *et al.* Loss of signaling via Gα13 in germinal center B cell-derived lymphoma. *Nature* **516**,  
776 254–258 (2014).
- 777 10. Oyler-Yaniv, A. *et al.* A Tunable Diffusion-Consumption Mechanism of Cytokine Propagation Enables  
778 Plasticity in Cell-to-Cell Communication in the Immune System. *Immunity* **46**, 609–620 (2017).
- 779 11. Ulvmar, M. H. *et al.* The atypical chemokine receptor CCRL1 shapes functional CCL21 gradients in lymph  
780 nodes. *Nat. Immunol.* **15**, 623–630 (2014).
- 781 12. Barmore, A. J. *et al.* Transferring the C-terminus of the chemokine CCL21 to CCL19 confers enhanced  
782 heparin binding. *Biochem. Biophys. Res. Commun.* **477**, 602–606 (2016).
- 783 13. Hasan, M., Najjam, S., Gordon, M. Y., Gibbs, R. V. & Rider, C. C. IL-12 is a heparin-binding cytokine. *J.*  
784 *Immunol. Baltim. Md 1950* **162**, 1064–1070 (1999).
- 785 14. Wrenshall, L. E., Platt, J. L., Stevens, E. T., Wight, T. N. & Miller, J. D. Propagation and control of T cell  
786 responses by heparan sulfate-bound IL-2. *J. Immunol. Baltim. Md 1950* **170**, 5470–5474 (2003).
- 787 15. Schumann, K. *et al.* Immobilized Chemokine Fields and Soluble Chemokine Gradients Cooperatively Shape  
788 Migration Patterns of Dendritic Cells. *Immunity* **32**, 703–713 (2010).
- 789 16. Handel, T. M. *et al.* Regulation of Protein Function by Glycosaminoglycans—as Exemplified by  
790 Chemokines. *Annu. Rev. Biochem.* **74**, 385–410 (2005).

- 791 17. Monneau, Y. R. *et al.* Solution structure of CXCL13 and heparan sulfate binding show that GAG binding site  
792 and cellular signalling rely on distinct domains. *Open Biol.* **7**, (2017).
- 793 18. Proudfoot, A. E. I. *et al.* Glycosaminoglycan binding and oligomerization are essential for the in vivo activity  
794 of certain chemokines. *Proc. Natl. Acad. Sci. U. S. A.* **100**, 1885–1890 (2003).
- 795 19. Proudfoot, A. E. I., Johnson, Z., Bonvin, P. & Handel, T. M. Glycosaminoglycan Interactions with  
796 Chemokines Add Complexity to a Complex System. *Pharmaceuticals* **10**, 70 (2017).
- 797 20. Stein, J. V. *et al.* The Cc Chemokine Thymus-Derived Chemotactic Agent 4 (Tca-4, Secondary Lymphoid  
798 Tissue Chemokine, 6ckine, Exodus-2) Triggers Lymphocyte Function–Associated Antigen 1–Mediated  
799 Arrest of Rolling T Lymphocytes in Peripheral Lymph Node High Endothelial Venules. *J. Exp. Med.* **191**,  
800 61–76 (2000).
- 801 21. Barinov, A. *et al.* Essential role of immobilized chemokine CXCL12 in the regulation of the humoral immune  
802 response. *Proc. Natl. Acad. Sci.* **114**, 2319–2324 (2017).
- 803 22. Fleury, M. E., Boardman, K. C. & Swartz, M. A. Autologous Morphogen Gradients by Subtle Interstitial  
804 Flow and Matrix Interactions. *Biophys. J.* **91**, 113–121 (2006).
- 805 23. Gunn, M. D. *et al.* A B cell-homing chemokine made in lymphoid follicles activates Burkitt’s lymphoma  
806 receptor-1. *Nature* **391**, 799–803 (1998).
- 807 24. Legler, D. F. *et al.* B cell-attracting chemokine 1, a human CXC chemokine expressed in lymphoid tissues,  
808 selectively attracts B lymphocytes via BLR1/CXCR5. *J. Exp. Med.* **187**, 655–660 (1998).
- 809 25. Lander, A. D. Morpheus Unbound: Reimagining the Morphogen Gradient. *Cell* **128**, 245–256 (2007).
- 810 26. Nibbs, R. J. B. & Graham, G. J. Immune regulation by atypical chemokine receptors. *Nat. Rev. Immunol.* **13**,  
811 815–829 (2013).
- 812 27. Zabel, B. A. *et al.* Chemoattractants, extracellular proteases, and the integrated host defense response. *Exp.*  
813 *Hematol.* **34**, 1021–1032 (2006).
- 814 28. Miller, H. *et al.* High-Speed Single-Molecule Tracking of CXCL13 in the B-Follicle. *Front. Immunol.* **9**,  
815 1073 (2018).
- 816 29. Ma, B., Jablonska, J., Lindenmaier, W. & Dittmar, K. E. J. Immunohistochemical study of the reticular and  
817 vascular network of mouse lymph node using vibratome sections. *Acta Histochem.* **109**, 15–28 (2007).
- 818 30. Wolf, M., Albrecht, S. & Märki, C. Proteolytic processing of chemokines: implications in physiological and  
819 pathological conditions. *Int. J. Biochem. Cell Biol.* **40**, 1185–1198 (2008).
- 820 31. Mortier, A., Van Damme, J. & Proost, P. Regulation of chemokine activity by posttranslational modification.  
821 *Pharmacol. Ther.* **120**, 197–217 (2008).
- 822 32. Novkovic, M. *et al.* Topological Small-World Organization of the Fibroblastic Reticular Cell Network  
823 Determines Lymph Node Functionality. *PLOS Biol* **14**, e1002515 (2016).
- 824 33. Watts, D. J. & Strogatz, S. H. Collective dynamics of ‘small-world’ networks. *Nature* **393**, 440–442 (1998).

- 825 34. Telesford, Q. K., Joyce, K. E., Hayasaka, S., Burdette, J. H. & Laurienti, P. J. The Ubiquity of Small-World  
826 Networks. *Brain Connect.* **1**, 367–375 (2011).
- 827 35. Phan, T. G., Grigorova, I., Okada, T. & Cyster, J. G. Subcapsular encounter and complement-dependent  
828 transport of immune complexes by lymph node B cells. *Nat. Immunol.* **8**, 992–1000 (2007).
- 829 36. Carrasco, Y. R. & Batista, F. D. B Cells Acquire Particulate Antigen in a Macrophage-Rich Area at the  
830 Boundary between the Follicle and the Subcapsular Sinus of the Lymph Node. *Immunity* **27**, 160–171 (2007).
- 831 37. Kislitsyn, A., Savinkov, R., Novkovic, M., Onder, L. & Bocharov, G. Computational Approach to 3D  
832 Modeling of the Lymph Node Geometry. *Computation* **3**, 222–234 (2015).
- 833 38. Deb, K. & Kalyanmoy, D. *Multi-Objective Optimization Using Evolutionary Algorithms*. (John Wiley &  
834 Sons, Inc., 2001).
- 835 39. Deb, K., Pratap, A., Agarwal, S. & Meyarivan, T. A fast and elitist multiobjective genetic algorithm: NSGA-  
836 II. *IEEE Trans. Evol. Comput.* **6**, 182–197 (2002).
- 837 40. Coelho, F. M. *et al.* Naive B cell trafficking is shaped by local chemokine availability and LFA-1–  
838 independent stromal interactions. *Blood* **121**, 4101–4109 (2013).
- 839 41. Miller, H. *et al.* Ultra-fast super-resolution imaging of biomolecular mobility in tissues. *bioRxiv* 179747  
840 (2017). doi:10.1101/179747
- 841 42. Gonzalez-Leal, I. J. *et al.* Cathepsin B in Antigen-Presenting Cells Controls Mediators of the Th1 Immune  
842 Response during Leishmania major Infection. *PLoS Negl. Trop. Dis.* **8**, e3194 (2014).
- 843 43. Mohamed, M. M. & Sloane, B. F. Cysteine cathepsins: multifunctional enzymes in cancer. *Nat. Rev. Cancer*  
844 **6**, 764–775 (2006).
- 845 44. Lemaire, R. *et al.* Selective induction of the secretion of cathepsins B and L by cytokines in synovial  
846 fibroblast-like cells. *Br. J. Rheumatol.* **36**, 735–743 (1997).
- 847 45. Batista, F. D. & Harwood, N. E. The who, how and where of antigen presentation to B cells. *Nat. Rev.*  
848 *Immunol.* **9**, 15–27 (2009).
- 849 46. Almeida, P. C. *et al.* Cathepsin B activity regulation. Heparin-like glycosaminoglycans protect human  
850 cathepsin B from alkaline pH-induced inactivation. *J. Biol. Chem.* **276**, 944–951 (2001).
- 851 47. Reddy, V. Y., Zhang, Q. Y. & Weiss, S. J. Pericellular mobilization of the tissue-destructive cysteine  
852 proteinases, cathepsins B, L, and S, by human monocyte-derived macrophages. *Proc. Natl. Acad. Sci. U. S. A.*  
853 **92**, 3849–3853 (1995).
- 854 48. Novkovic, M., Onder, L., Bocharov, G. & Ludewig, B. Graph Theory-Based Analysis of the Lymph Node  
855 Fibroblastic Reticular Cell Network. *Methods Mol. Biol. Clifton NJ* **1591**, 43–57 (2017).
- 856 49. Bjørnstad, null, Ims, null & Lambin, null. Spatial population dynamics: analyzing patterns and processes of  
857 population synchrony. *Trends Ecol. Evol.* **14**, 427–432 (1999).
- 858 50. Moran, P. A. P. Notes on Continuous Stochastic Phenomena. *Biometrika* **37**, 17–23 (1950).

859 51. Plank, M., Wadhams, G. H. & Leake, M. C. Millisecond timescale slimfield imaging and automated  
860 quantification of single fluorescent protein molecules for use in probing complex biological processes. *Integr.*  
861 *Biol. Quant. Biosci. Nano Macro* **1**, 602–612 (2009).

862 52. Miller, H., Zhou, Z., Wollman, A. J. M. & Leake, M. C. Superresolution imaging of single DNA molecules  
863 using stochastic photoblinking of minor groove and intercalating dyes. *Methods San Diego Calif* **88**, 81–88  
864 (2015).

865 53. Reyes-Lamothe, R., Sherratt, D. J. & Leake, M. C. Stoichiometry and architecture of active DNA replication  
866 machinery in Escherichia coli. *Science* **328**, 498–501 (2010).

867 54. Leake, M. C. *et al.* Stoichiometry and turnover in single, functioning membrane protein complexes. *Nature*  
868 **443**, 355–358 (2006).

869 55. Leake, M. C., Wilson, D., Bullard, B. & Simmons, R. M. The elasticity of single kettin molecules using a  
870 two-bead laser-tweezers assay. *FEBS Lett.* **535**, 55–60 (2003).

871 56. Leake, M. C. *et al.* Variable stoichiometry of the TatA component of the twin-arginine protein transport  
872 system observed by in vivo single-molecule imaging. *Proc. Natl. Acad. Sci. U. S. A.* **105**, 15376–15381  
873 (2008).

874 57. Wollman, A. J. M. & Leake, M. C. Millisecond single-molecule localization microscopy combined with  
875 convolution analysis and automated image segmentation to determine protein concentrations in complexly  
876 structured, functional cells, one cell at a time. *Faraday Discuss.* **184**, 401–424 (2015).

877 58. Stracy, M. *et al.* Single-molecule imaging of DNA gyrase activity in living Escherichia coli. *Nucleic Acids*  
878 *Res.* (2018). doi:10.1093/nar/gky1143

879 59. Robson, A., Burrage, K. & Leake, M. C. Inferring diffusion in single live cells at the single-molecule level.  
880 *Philos. Trans. R. Soc. Lond. B. Biol. Sci.* **368**, 20120029 (2013).

881 60. Cosgrove, J. *et al.* Agent-Based Modeling in Systems Pharmacology. *CPT Pharmacomet. Syst. Pharmacol.*  
882 n/a-n/a (2015). doi:10.1002/psp4.12018

883 61. Macal, C. M. & North, M. J. Tutorial on agent-based modelling and simulation. *J. Simul.* **4**, 151–162 (2010).

884 62. McKay, M. D., Beckman, R. J. & Conover, W. J. A Comparison of Three Methods for Selecting Values of  
885 Input Variables in the Analysis of Output from a Computer Code. *Technometrics* **21**, 239–245 (1979).

886 63. Alden, K. *et al.* Spartan: a comprehensive tool for understanding uncertainty in simulations of biological  
887 systems. *PLoS Comput. Biol.* **9**, e1002916 (2013).

888 64. Bishop, C. M. *Neural Networks for Pattern Recognition*. (Clarendon Press, 1996).

889 65. Moepps, B. & Thelen, M. Chapter Five - Monitoring Scavenging Activity of Chemokine Receptors. in  
890 *Methods in Enzymology* (ed. Handel, T. M.) **570**, 87–118 (Academic Press, 2016).

891 66. Clark-Lewis, I., Vo, L., Owen, P. & Anderson, J. Chemical synthesis, purification, and folding of C-X-C and  
892 C-C chemokines. in *Methods in Enzymology* **287**, 233–250 (Academic Press, 1997).

- 893 67. von Tscharner, V., Prod'homme, B., Baggiolini, M. & Reuter, H. Ion channels in human neutrophils activated  
894 by a rise in free cytosolic calcium concentration. *Nature* **324**, 369–372 (1986).
- 895 68. Hauser, M. A. *et al.* Inflammation-Induced CCR7 Oligomers Form Scaffolds to Integrate Distinct Signaling  
896 Pathways for Efficient Cell Migration. *Immunity* **44**, 59–72 (2016).
- 897 69. Schaeuble, K. *et al.* Ubiquitylation of the chemokine receptor CCR7 enables efficient receptor recycling and  
898 cell migration. *J. Cell Sci.* **125**, 4463–4474 (2012).
- 899 70. Vargha, A. & Delaney, H. D. A Critique and Improvement of the 'CL' Common Language Effect Size  
900 Statistics of McGraw and Wong. *J. Educ. Behav. Stat.* **25**, 101–132 (2000).
- 901



**Acknowledgements:** We wish to thank Antal Rot, Paul Kaye, Dimitris Lagos and members of the York Computational Immunology Laboratory for advice and reagents, the York Teaching Hospital NHS Foundation Trust R&D Department for invaluable assistance with sample collection protocol and Imaging & Cytometry Laboratory staff for technical input. Work was funded by the Swiss National Science Foundation Grant (310030\_163336) to MT and Swiss national Science Foundation Grants 159188 and 166500 to BL. MCL was supported by the Biological Physical Sciences Institute (BPSI), Medical Research Council grants MR/K01580X/1 (MCL), MC\_PC\_15073 (MCC, MCL and ZZ) and BBSRC grants BB/N006453/1 and BB/R001235/1 (MCL). MW was supported by the Bernische Krebsliga to MW and SA, by the Swiss European Union FP6 (INNOCHEM, LSHB-CT-2005-518167), the Swiss National Science Foundation (143718 to MU) and the San Salvatore Foundation to MU, the Swiss National Science Foundation (169936) to DL. DV was supported by the MD/PhD scholarship from the Swiss National Science Foundation and the Max Cloëtta Foundation (313600-115688). BM was supported by INSERM U1151. KA was supported by Wellcome Trust Centre for Future Health grant (204829), JT by EPSRC grant EP/K040820/1. JC, JT and MCC were funded by Wellcome Trust (Computational Approaches in Translational Science WT0905024MA, HFSP (RGP0006/2009 TC and MCC) and Medical Research Grants MR/K021125/1 and G0601156. MCC is funded by the Kennedy Trust.

**Author Contributions:**

JC, MN designed and performed the experiments, analyzed and interpreted the data and wrote the manuscript; SA, NBP, ZZ, LO, UM, JC, HM, KA, AT, SJ, ET, DV, MH, MU, CL, AC, POT, RP, WGP & DL, performed experiments, analyzed data, provided key reagents, intellectual input and technical assistance; MT, TC, BM, J.S., M.W.: designed experiments and analyzed data, MW, MCL, JT, BL and MCC: designed experiments, analyzed and interpreted results, coordinated the research and wrote the paper.

**Competing Interests:**

The Authors declare no competing interest.

## 929 **Figure Legends**

930

### 931 **Figure 1. The topological network properties of CXCL13<sup>+</sup> follicular stromal cells.** (A)

932 Mapping confocal images of lymph node follicles taken from Cxcl13-cre/EYFP reporter mice  
933 using the Imaris image analysis software. The FDC sub-network is highlighted in yellow and  
934 the RC sub-network in cyan. Distributions of degree centrality, edge length and local  
935 clustering coefficient are indicated for the FDC and RC sub-networks (B-D). (E) Distribution  
936 of shortest path lengths is indicated for the global follicular network and are compared to that  
937 of an equivalent random network with the same number of nodes and edges (F). Data  
938 represent mean  $\pm$  SD for n = 4 mice. Statistical significance was determined using a Two-way  
939 ANOVA with Sidak's multiple comparison test. \* p < 0.05, \*\* p < 0.01, \*\*\* p < 0.001. Scale  
940 bar = 50  $\mu$ m. Source data are provided as a Source Data file.

941

### 942 **Figure 2. Mapping CXCL13 spatial distribution through simulation analysis and**

943 **multiobjective optimization.** (A) Overview of the multiscale model platform. In this  
944 modular system stromal cells are modelled as a graph (Module 1), chemokine diffusion is  
945 modelled as a discretised partial differential equation (Module 2), while B cells are modelled  
946 as agents which can interact with their local environment through a set of coupled differential  
947 equations and vector based calculations (Module 3). (B) Example structure of an artificial  
948 neural network used to emulate CXCL13Sim. The network has 13 input nodes that connect to  
949 3 hidden layers, and a single output node predicting the meandering index. A distinct network  
950 is created for each simulator output. The hyperparameters of the network were determined  
951 using K-folds cross validation. (C) The *in silico* follicular stromal network with a chemotactic  
952 landscape created for model 1 and model 2 by the network (D) Comparison of scanning rates  
953 *in silico* for Model 1 and Model 2. Each parameter set was run 200 times with significance  
954 assessed using the Vargha-Delaney A-test<sup>70</sup>. The test statistic (0.99) exceeds the threshold for  
955 a large effect size (0.71). Bar plots represent the median value for the emergent scanning rate

and the error bars represent the I.Q.R (E) Parameter distributions for diffusion and decay rates corresponding to the Pareto optimal solutions shown in F with calibrated values for each parameter shown using the dotted red line. (F) Using a MOEA scheme we seek to address the following 4 objectives: minimize the root mean squared error between emulator and simulator responses for cell speed, meandering index and motility coefficient; and maximize scanning rates. The Pareto front of solutions represents the trade off in performance between cell behaviors and scanning rates, using NSGA-II (emulation pipeline described in **Supplementary Figure 1**). Source data are provided as a Source Data file.

**Figure 3. CXCL13 interactions with ECM components constrain mobility** (A) tonsil tissue sections were stained with anti-CD19 and anti-heparan sulphate antibodies. Following incubation in PBS or heparinase II treatment binding of CXCL13<sup>AF647</sup> to the B follicle was assessed (B) quantification of total fluorescent intensity for each image. Shapiro-Wilk tests indicated that the datasets were not normally distributed (p-value < 0.001) and so significance was assessed using a Mann Whitney U test (p-value < 0.001). Data shown is from a single experiment (from a total of 2 independent experiments) with each data point representing a distinct follicle obtained from a single patient. (C) Quantification of CXCL13<sup>AF647</sup> mobility in CD19<sup>+</sup> positive regions of human tonsil sections. Diffusion measured in untreated tissue sections is indicated in red with values obtained heparinase II treated sections indicated in blue. All tissue sections were obtained from the same patient. The median [I.Q.R] diffusion rate of CXCL13<sup>AF647</sup> in untreated sections was calculated as 0.19 [0.001-0.79]  $\mu\text{m}^2\text{s}^{-1}$ , while treatment with heparinase-II led to a significantly different (assessed using the Mann-Whitney U test) diffusion coefficient of 1.6 [0.47-3.9]  $\mu\text{m}^2\text{s}^{-1}$  (P < 0.0001). (D) Characterizing the multiple modes of diffusion observed in our single molecule tracking analysis in B-follicles treated with heparinase II, or PBS. Source data are provided as a Source Data file.

982 **Figure 4. Analyzing the spatial distribution of the immobile CXCL13 fraction** (A) IHC  
 983 staining of the FDC marker CD35 (green) and CXCL13 (red) in human lymph nodes and  
 984 tonsils. (B) The spatial autocorrelation of CXCL13 expression in samples from one patient,  
 985 each line represents the spatial autocorrelation for a distinct follicle (C) Comparison of the  
 986 distances at which no statistically significant spatial autocorrelation (determined using  
 987 permutation testing as described in the Materials and Methods) was detected in human tonsils,  
 988 and for model 1 and model 2. Each data point represents the distance at which no statistically  
 989 significant spatial autocorrelation was observed for the intensity of anti-CXCL13 staining in a  
 990 distinct tonsil follicle, with data pooled from 5 different patients. The red line represents the  
 991 median distance for each group with significance the human dataset and each simulation  
 992 model (run with 200 repeat executions) assessed using the Mann Whitney U test (p-value <  
 993 0.06 for model 1 and  $p < 0.001$  for model 2). Source data are provided as a Source Data file.  
 994

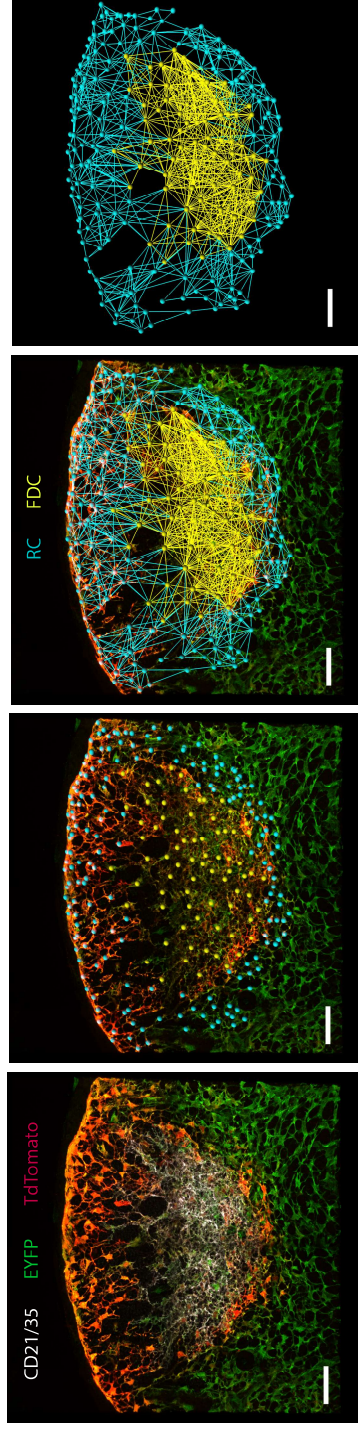
995 **Figure 5. Cathepsin B mediated processing of CXCL13** (A) 4  $\mu$ M CXCL13 was incubated  
 996 with 72 nM Cath-B for the indicated times at 37°C. The cleavage products were separated by  
 997 SDS-PAGE and stained with Coomassie blue. (B) C-terminal truncation of CXCL13 by Cath-  
 998 B leads to decreased heparin binding. CXCL13 was incubated for 3h with Cath-B, the  
 999 reaction stopped, and the sample supplemented with intact CXCL13 and subsequently loaded  
 1000 on a Hitrap<sup>TM</sup> heparin column. Proteins were eluted with a NaCl gradient of 0 to 1.0 M and  
 1001 absorbance measured at 280 nm. The three peaks were allocated as Cath-B (1), CXCL13<sup>[1-72]</sup>  
 1002 (2) and CXCL13 (3). (C) Processing of CXCL13 by Cath-B at pH 6.8 was unaffected by the  
 1003 presence of 5- or 10-fold (w/w) excess heparin sulfate, hyaluronic acid or chondroitin sulfate.  
 1004 (D) Representative  $[Ca^{2+}]_i$  -dependent fluorescence changes in fura-2 loaded CXCR5-  
 1005 transfected Pre-B 300-19 cells induced by 30 nM CXCL13 or CXCL13<sup>[1-72]</sup>. (E) Dose  
 1006 response of calcium mobilization elicited by CXCL13 and CXCL13<sup>[1-72]</sup>. Relative units (mean  
 1007  $\pm$  SD) were calculated as described in Methods. (F) CXCR5 surface expression after  
 1008 incubation of CXCR5-transfected Pre-B 300-19 cells with CXCL13 and CXCL13<sup>[1-72]</sup>.

1009 CXCR5 expression levels were quantified by flow cytometry analysis. Data (mean  $\pm$  SD)  
 1010 from at least four independent experiments show the percentage of surface CXCR5 compared  
 1011 to control. (G) Primary human B cell migration in response to intact and truncated CXCL13  
 1012 was evaluated using 5  $\mu$ m pore size Transwell filters. Data represents the percentage of  
 1013 migrated cells relative to the number of cells added to the Transwell filters. Values (mean  $\pm$   
 1014 SD) represent at least three independent experiments. Statistically significant differences  
 1015 (determined using a Students T-test) are indicated, \* $p < 0.05$  and \*\*  $p < 0.01$ . (H) co-  
 1016 localisation of Cath-B (red) and CD68 (green) signal in tonsil follicles. (H) Co-localisation of  
 1017 Cath-B and CD68 staining in the B-follicle through immunohistochemistry analysis (I)  
 1018 Analysis of Cath-B (Red), CD4+ T cells (brown) and CXCL13 in the B cell follicle and  
 1019 germinal center reaction. Source data are provided as a Source Data file.

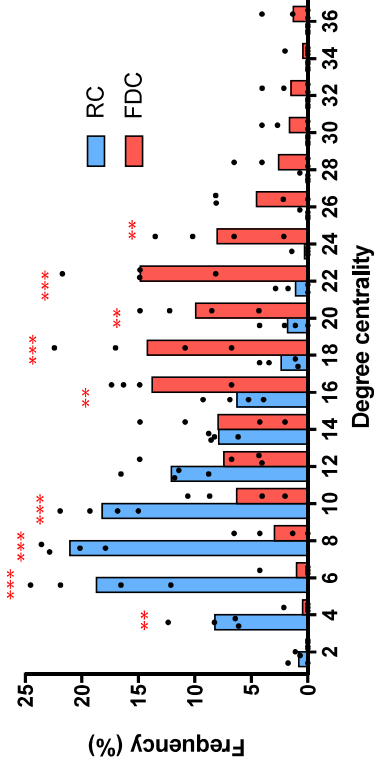
1020  
 1021 **Figure 6. Cathepsin B deficient mice have abnormal follicle architecture** (A) Analysis of  
 1022 lymph node presence and morphology from WT and *Ctsb*<sup>-/-</sup> lymph nodes. (B) Percentage of  
 1023 B cells, CD4+ and CD8+ T cells in WT and *Ctsb*-deficient LNs determined using flow  
 1024 cytometry, with significance assessed using a Student's T-test (C) Staining of WT and *Ctsb*<sup>-/-</sup>  
 1025 LNs with anti-B220 (B cells), anti-Podoplanin (Stroma), anti-CD4 (T cells) and anti-CD21/35  
 1026 (Follicular Dendritic Cells). (D) Staining of WT and *Ctsb*<sup>-/-</sup> LNs for CD19 (B cells) and  
 1027 Meca-79 (PNAd+ HEVs). (E) Entry of CFSE transferred WT B cells into the LN parenchyma  
 1028 of either WT or *Ctsb*<sup>-/-</sup> recipient mice was assessed by confocal microscopy. (F) Ratio of LN  
 1029 entry of KO:WT B cells into either WT or *Ctsb*<sup>-/-</sup> recipients. To determine the relative  
 1030 efficiency of WT vs *Ctsb*<sup>-/-</sup> B cells to enter into WT or *Ctsb*<sup>-/-</sup> recipients equal numbers of  
 1031 CSFE (ThermoFisher) labelled KO cells and CMTMR (ThermoFisher) labelled WT cells  
 1032 were transferred into corresponding recipient mice. The ratio of transferred B (B220<sup>+</sup>) cells  
 1033 KO:WT was calculated by taking into account the relative efficiency of CFSE and CMTMR  
 1034 labelled survival post transfer by calculating the ratio of WT CSFE:WT CMTMR transferred  
 1035 cells. (G) Quantification of migrated CSFE positive B cells by flow cytometry. (H) Analysis  
 1036 of *Cxcl13* and *Cxcr5* mRNA expression from total LN from WT and *Ctsb* deficient mice

1037 using RT-qPCR. For figures F-H significance was assessed using a student's T-test with p-  
1038 values provided for each comparison. Source data are provided as a Source Data file.

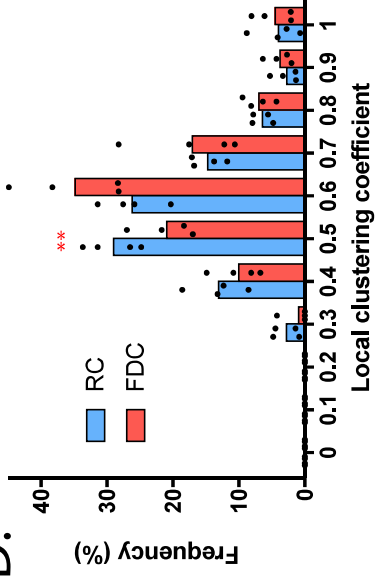
A.



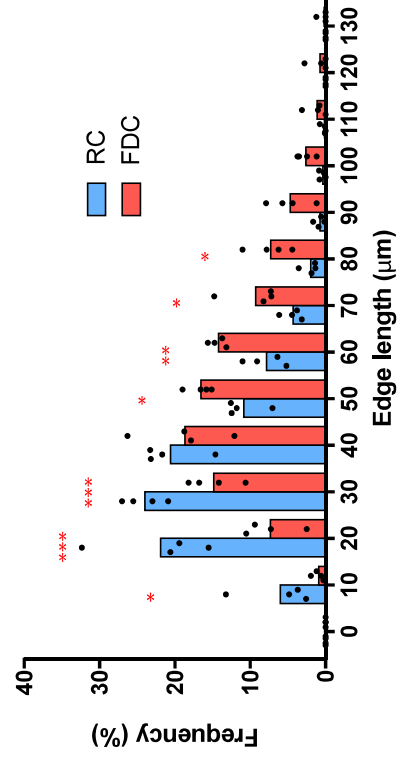
B.



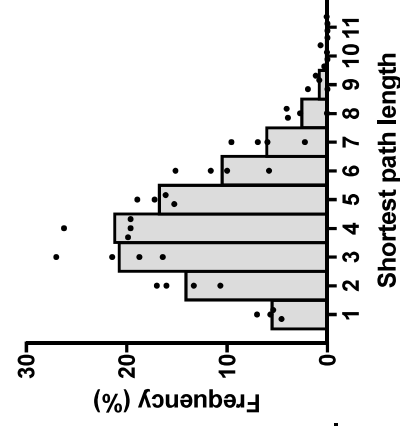
D.



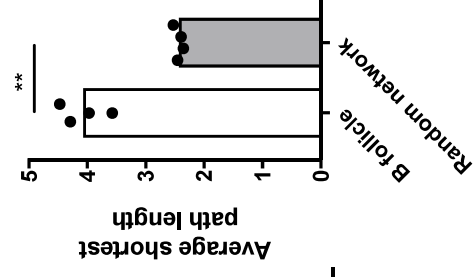
C.

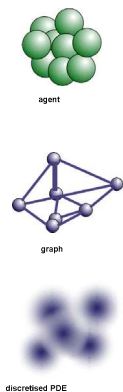
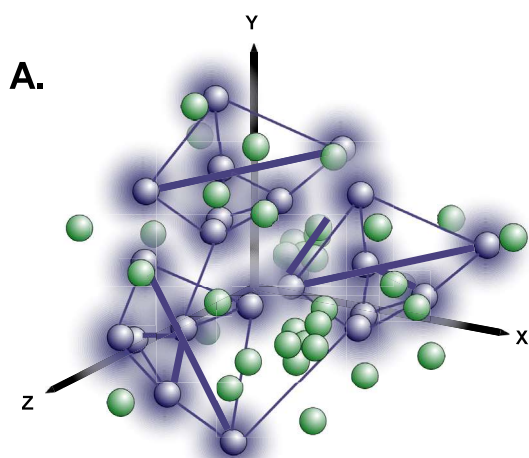


E.

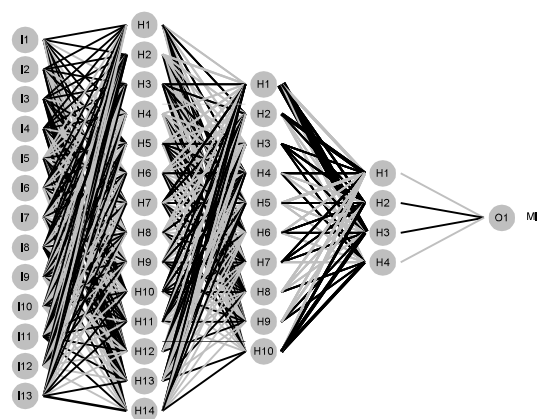


F.

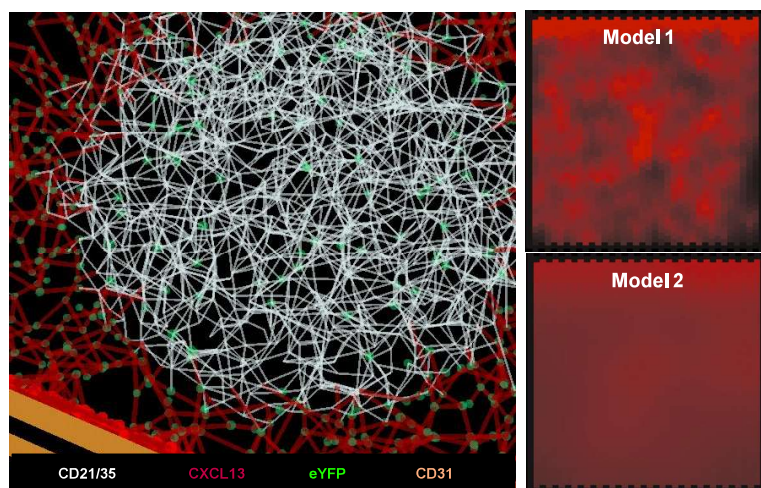




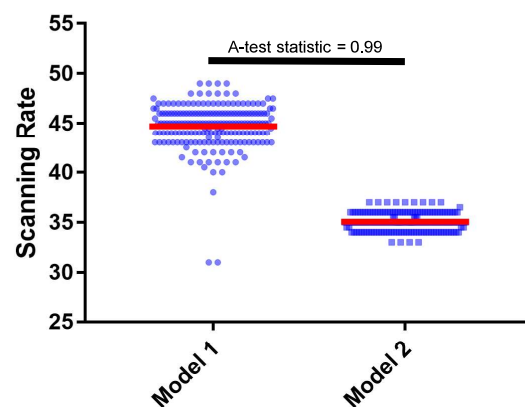
**B.**



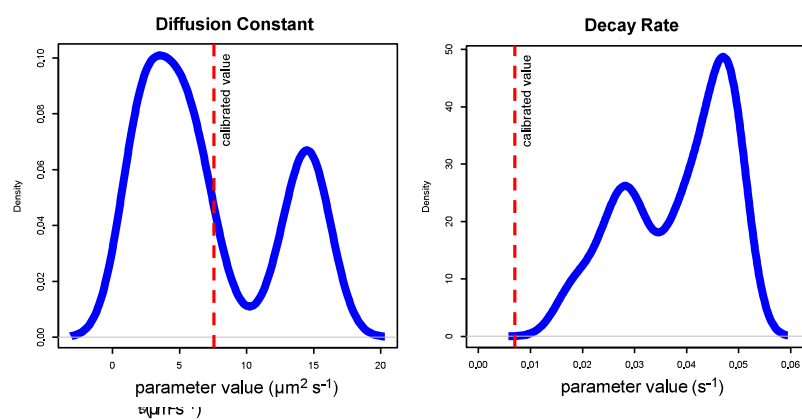
**C.**



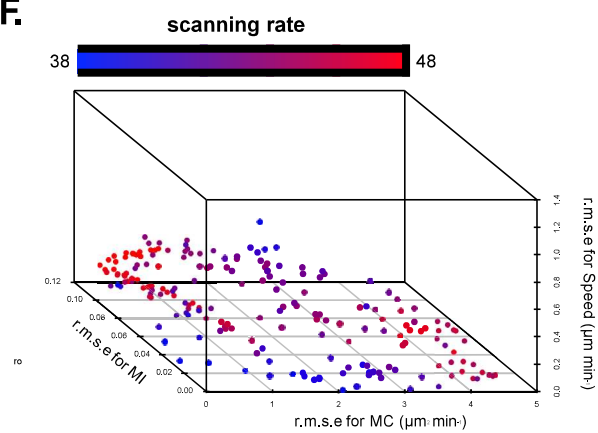
**D.**



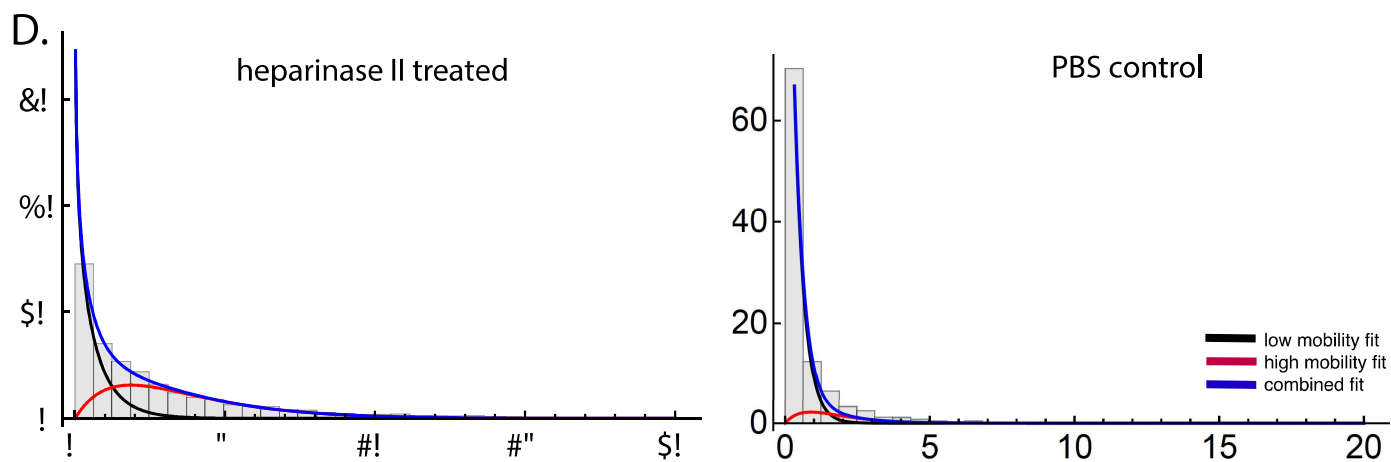
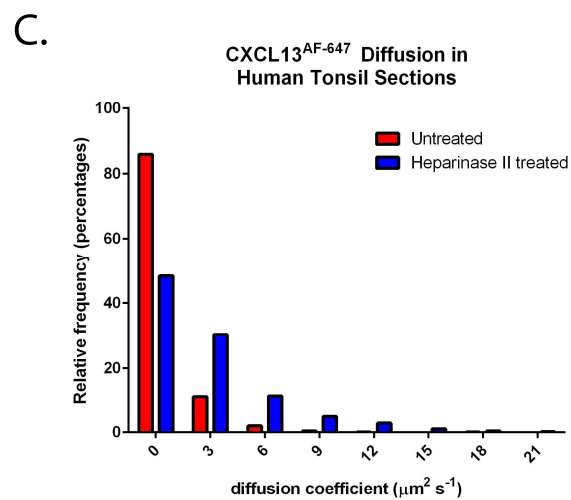
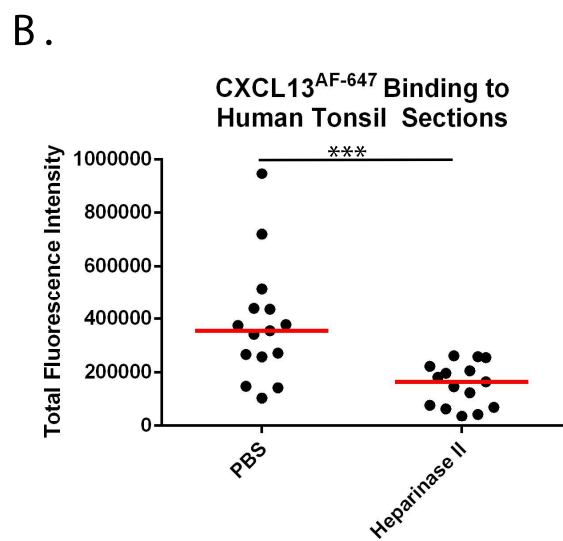
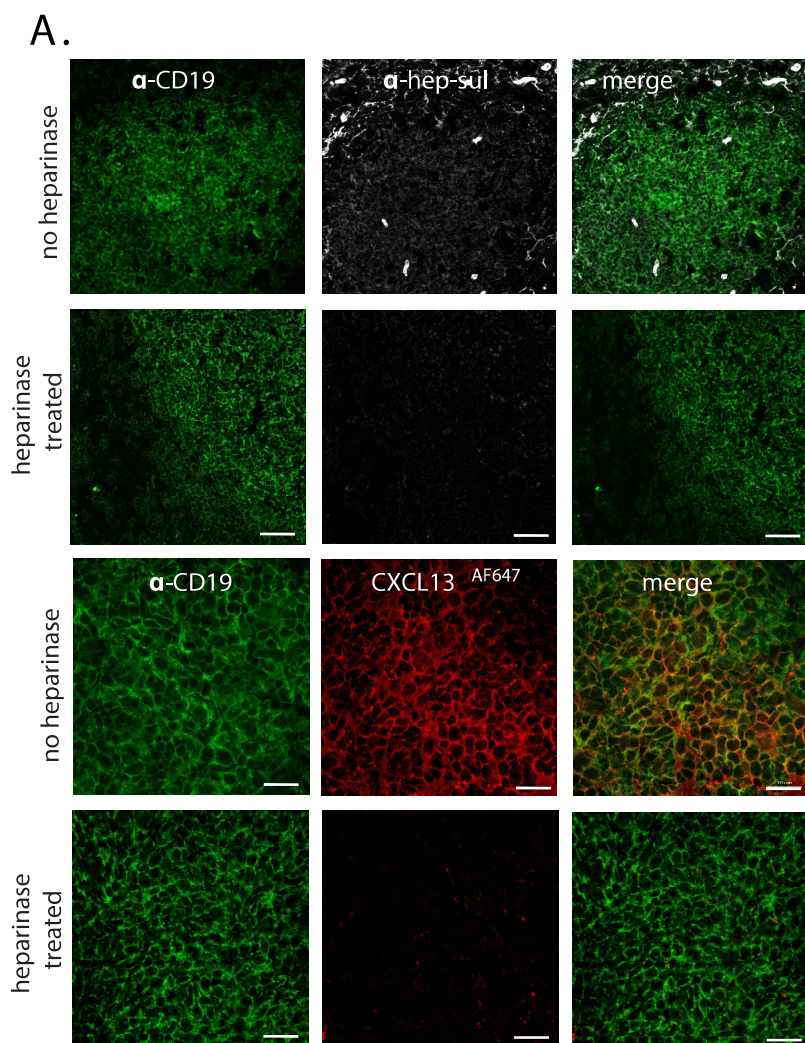
**E.**

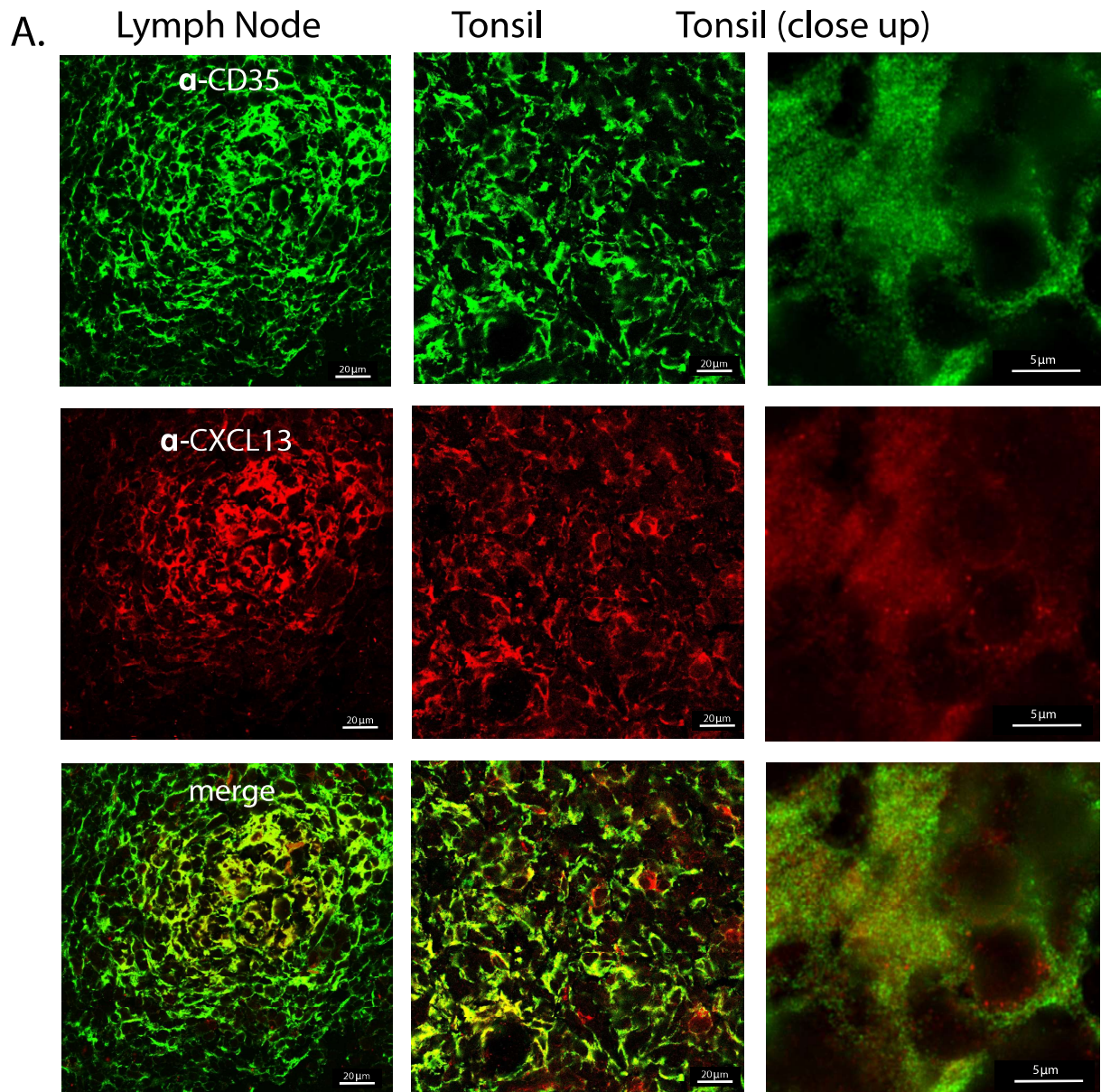


**F.**

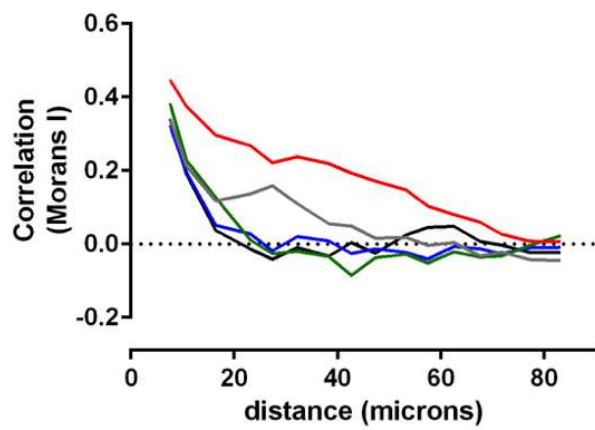




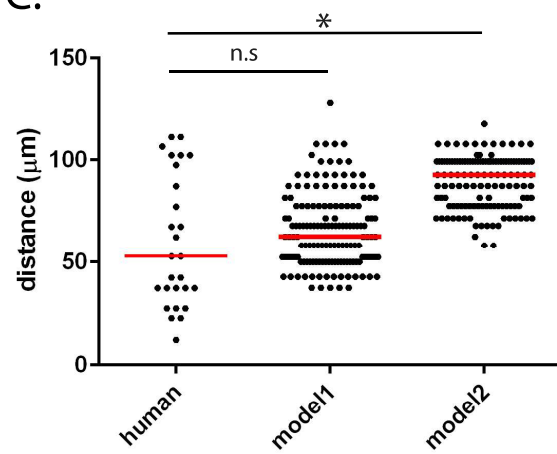




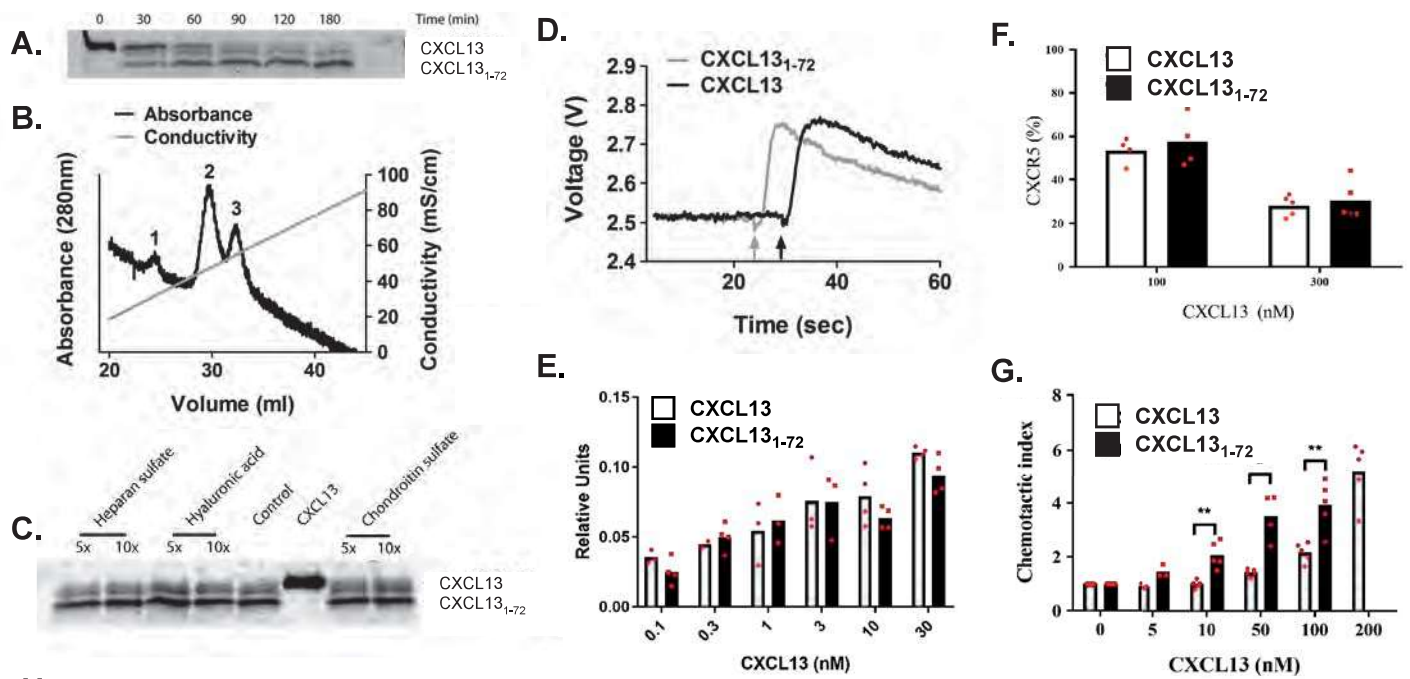
B.



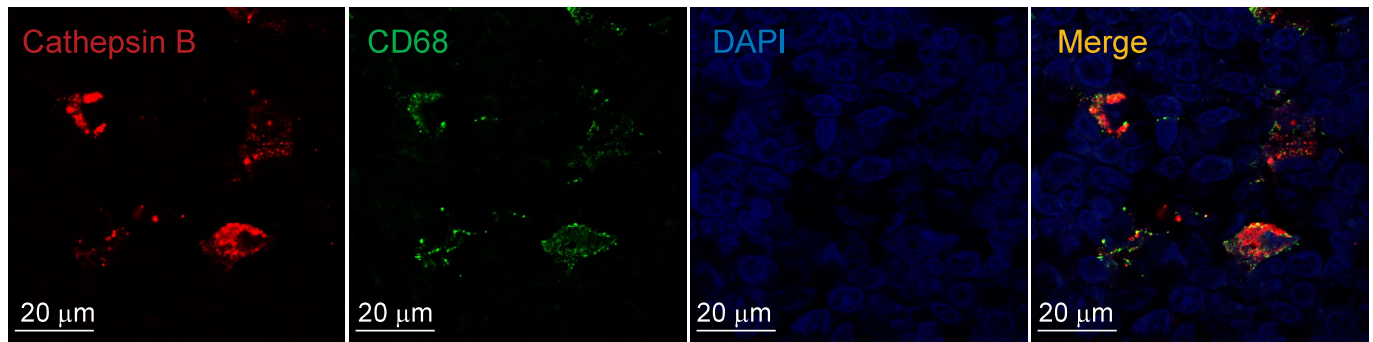
C.







**H.**



**I.**

